

Reconstruction of Gamma-ray Direction using Boosted Decision Trees and the *Disp* Parameter

Sreela Das

Department of Physics

McGill University

Montréal, Québec

September 26, 2019

A thesis submitted to McGill University in partial fulfillment of the
requirements of the degree of Master of Science

© Sreela Das, 2019

Acknowledgments

I would like to thank my supervisor, Prof. Kenneth Ragan for his guidance, advice and feedback for this work. I would also like to thank Tony Lin, for his work on the analysis package that enabled the work in this thesis. Thanks are also due to Prof. David Hanna, Benjamin Zitzer, Thomas Rosin, Matthew Lundy, Emma Ellingwood, Stephan O'Brien, and Sajan Kumar for their insights, discussions and constructive criticisms. Many thanks also to Paul Mercure and Juan Gallego for their technical assistance with the computer systems. Lastly, I would like to thank my family and friends for their love and support.

Abstract

The geometric reconstruction of shower direction at the VERITAS imaging atmospheric Cherenkov telescope (IACT) system sees a substantial degradation at large zenith angles ($\phi > 45^\circ$). A machine-learning-based reconstruction of this direction is not expected to suffer from the same limitations because it does not rely on the geometry of the observation. In this work, we demonstrate the predicted efficiency of a shower direction reconstruction using boosted decision trees. We also test how well this translates to a data analysis by performing a proof of concept with compact and point-source objects.

Abrégé

La reconstruction géométrique de direction de cascades de particules au système d'imagerie télescopique Cherenkov (IACT) de VERITAS souffre d'une dégradation substantielle aux grands angles zénithiques ($\phi > 45^\circ$). Une reconstruction basée sur l'apprentissage machine ne devrait pas souffrir des mêmes limitations car elle ne compte pas sur la géométrie de l'observation. Dans ce travail, nous démontrons l'efficacité prévue d'une reconstruction de direction de cascades à l'aide de Boosted Decision Trees optimisés. Nous testons également dans quelle mesure cela se traduit par une analyse de données en effectuant une validation de principe avec des objets compacts et à source ponctuelle.

Statement of Original Contribution

Elements of this thesis that constitute original contributions of the author are:

- Generating new *Disp* tables with various different parameters (Chapters 2 and 3).
- Study of the effect of various parameters on the training of BDTs (Chapter 3).
- Study of the effect of various parameters on the performance of BDTs (Chapter 3).
- Comparison of the results from simulations to those from data (Chapter 3).

In addition to this I have contributed to VERITAS operations through trips on-site for operations during observing runs as well as off-site data quality management shifts.

Contents

Acknowledgments	i
Abstract	ii
Abrégé	iii
Statement of Original Contribution	iv
Contents	v
List of Figures	viii
List of Tables	x
1 Introduction	1
1.1 Gamma Ray Astrophysics	1
1.1.1 Ground Based Gamma-Ray Astrophysics	2
1.2 VERITAS Overview	3
1.2.1 Gamma-Ray Initiated Extensive Air Showers	4
1.2.2 Cherenkov Radiation	4
1.2.3 Imaging Atmospheric Cherenkov Telescopes	7
1.2.4 The VERITAS Instrument	9
1.3 Shower Image Parameters	12
1.3.1 The <i>Disp</i> Parameter	12

2 Simulation and Analysis Packages	15
2.1 Overview	15
2.2 Shower Generation	16
2.3 The VEGAS Analysis Package	17
2.4 Direction Reconstruction	19
2.4.1 The <i>Disp</i> Method	19
2.5 Boosted Decision Trees	21
2.5.1 Training	24
2.5.2 Boosting	24
2.5.3 Testing	24
2.6 Noise in Simulations	25
3 Analysis Methods	26
3.1 Preliminary Test and Motivation	26
3.2 <i>Disp</i> Table and R_{68} Dependencies	29
3.2.1 Zenith Angle Dependence	29
3.2.2 Over-training	31
3.2.3 Noise Related Effects	34
3.2.4 Higher Statistics Tables	35
3.2.5 Acceptance Correction for Offset from Camera Center	36
3.2.6 Energy Dependence	40
3.3 R_{68} for Observational Data and Known Objects	41
3.3.1 Data Constraints and Li & Ma Significance	42
3.3.2 R_{68} for the Crab Nebula	45
3.3.3 R_{68} for Mrk421	49
4 Conclusions	52
4.1 Summary	52
4.2 Future Work	53

Bibliography**54**

List of Figures

1.1	Photograph of the VERITAS telescopes and the control center.	3
1.2	Processes involved in generating extensive air showers.	5
1.3	Mechanism of Cherenkov radiation.	6
1.4	Illustration of an IACT array.	8
1.5	Gamma-ray EAS at a telescope array.	9
1.6	PMTs in the VERITAS camera.	10
1.7	The image axis parameter.	13
1.8	The Hillas ellipse.	13
1.9	The Disp Parameter.	14
2.1	Stereoscopic reconstruction at LZA.	20
2.2	Angular resolution of Method0.	21
2.3	Combining multiple telescopes in <i>Disp</i> reconstruction.	22
2.4	An example of a BDT	23
3.1	Gaussian shape of the simulation deviation.	27
3.2	R_{68} from the Gaussian fit and the numerical integral.	28
3.3	Crab direction reconstruction using Method0.	29
3.4	“standard” <i>Disp</i> table reconstruction.	30
3.5	Small <i>Disp</i> table reconstruction (noise = 250 MHz).	31
3.6	Over-training test.	33
3.7	<i>Disp</i> table reconstruction vs noise.	34

3.8	Higher statistics <i>Disp</i> table reconstruction vs noise.	36
3.9	Weight functions for offset from camera center.	37
3.10	R_{68} for the acceptance correction functions.	39
3.11	Energy Dependence of Method0.	40
3.12	Energy Dependence of the old Method5t.	41
3.13	Energy Dependence of the new Method5t.	42
3.14	Energy and zenith dependence of the new Method5t.	43
3.15	Energy and zenith dependence of Method0 and the old Method5t	43
3.16	Performance of the new <i>Disp</i> method compared to Method0 and the old <i>Disp</i> method	44
3.17	Crab skymaps using the new <i>Disp</i> tables.	46
3.18	Crab (horizon-to-horizon runs) direction reconstruction using Method5t.	47
3.19	Crab (LZA runs) direction reconstruction using Method5t.	48
3.20	Mrk421 skymaps using the new <i>Disp</i> tables.	50
3.21	Mrk421 direction reconstruction using Method5t.	51

List of Tables

Chapter 1

Introduction

1.1 Gamma Ray Astrophysics

Gamma-ray astrophysics studies the physics and the sources of particles at high energies ($E > 1$ GeV). While astronomy is a centuries-old science, gamma-ray astrophysics has only come into play since the advent of satellite technology and subsequently of Imaging Atmospheric Cherenkov Telescopes (IACTs) in the 1980s [1][2]. Due to constraints from atmospheric interactions, direct detection of high energy astrophysical emissions is not feasible with traditional ground-based instruments. Satellites are able to circumvent these issues by being high in the atmosphere and intercepting particles prior to these interactions. IACTs are able to use them to their benefit by using the (lower-energy) products of these atmospheric interactions to reconstruct the incident particles which themselves would be too energetic to be detected by the instrument.

High-energy (HE, $E > 1$ GeV) or very high energy (VHE, $E > 100$ GeV) gamma-ray emission is a signature of extreme astrophysical processes like relativistic jets and strong electromagnetic fields [3]. These processes are among the most energetic phenomena in the universe and are present in active galactic nuclei (AGN), pulsar wind nebulae (PWN), and

pulsars. Since the penetration depth for higher energy photons in the atmosphere is shorter than their optical counterparts, they become much harder to manipulate using conventional methods used for photons. Instead, methods of high-energy particle physics and detector technology used for other high-energy particles are used for gamma-ray detection – in this case using the atmosphere as an electromagnetic calorimeter. Satellite-based instruments like the Fermi Large Area Telescope (LAT) are able to detect lower-energy gamma rays (30 MeV – 100 GeV) directly through tracking pair production e^+/e^- pairs, but for VHE gamma rays ($E > 100$ GeV) the much lower photon flux means that effective areas required for significant statistics are much larger, and not feasible for satellite-based instruments.

1.1.1 Ground Based Gamma-Ray Astrophysics

The Whipple Collaboration [2] pioneered the technique for indirect detection of gamma rays through the collection of Cherenkov photons emitted from extensive air showers generated from high-energy photon interactions with the atmosphere. The direction of the primary photons can be determined by imaging the air showers with telescopes. This also enables the rejection of hadronic showers from cosmic rays and provides an effective area much larger than is possible with space-based instruments. Cherenkov light used to detect these showers arrives in a region with a radius of ~ 100 m. The current generation of IACTs uses multiple telescopes which provide better sensitivity, better hadronic rejection and larger effective areas than individual telescopes [4]. In the thirty years of ground-based gamma ray astrophysics, over 200 VHE sources have been detected [5].

The current generation of ground based gamma-ray observatories includes three major telescope arrays. The MAGIC array [6], located on the Canary Islands of La Palma, Spain consists of two IACTs with 17 m diameter reflectors. The H.E.S.S. array [7] in the Khomas Highlands of Namibia, is an array of five IACTs, four of which have 13 m diameter reflectors while the fifth, in the center of the array has a 28 m reflector. The VERITAS

array [8] in Arizona, USA, the subject of this thesis, is an array of four telescopes, each with reflectors 12 m in diameter [9].

1.2 VERITAS Overview

The Very Energetic Radiation Imaging Telescope Array System (VERITAS) [10] is an array of four IACTs at the Fred Lawrence Whipple Observatory in southern Arizona (shown in Fig. 1.1), which started operating in 2007. Gamma rays are detected through imaging Cherenkov radiation emitted from relativistic charged particles (primarily e^+/e^-) in air showers initiated by VHE gamma rays. This section contains a brief description of the instrument and the technique used in this experiment. After the moving of one telescope in 2009, and upgrading the camera to higher quantum efficiency photo-multiplier tubes (PMTs) in 2012, VERITAS is sensitive to an energy range between $\sim 85\text{GeV}$ and $\sim 30\text{TeV}$ and has a field of view of 3.5° .



Figure 1.1: Photograph of the VERITAS telescopes and the control center. Photo taken from [8].

1.2.1 Gamma-Ray Initiated Extensive Air Showers

At gamma-ray energies, photons interact with the upper atmosphere resulting primarily in pair production of e^+/e^- pairs as shown in Fig. 1.2. On propagating through the atmosphere, electrons/positrons undergo “bremsstrahlung” and emit gamma rays.

“Bremsstrahlung”, German for “breaking radiation”, is a process where a charged particle (in this case an electron/positron) accelerated in the electromagnetic field of a nucleus loses energy by emitting photons. The bremsstrahlung photons can again undergo pair production and the shower continues as before resulting in an exponentially growing number of particles, with a decreasing mean particle energy.

Higher energy particles are beamed more strongly forward and so in the VHE gamma-ray energy scale, the particle shower has a small footprint (~ 30 m) transverse to the direction of the initiating particle, and a large longitudinal distribution (~ 10 km). As the shower proceeds, the mean energy of the particles gets progressively smaller, due partly to division among a larger number of particles and partly due to loss to ionization. Eventually, the process reaches an energy where Compton scattering becomes the dominant process causing energy loss, and the cascade stops. At this point, the shower energy dissipates into the atmosphere through ionization. Since the cascade which was so far growing exponentially halts here, the number of particles does not increase beyond this point and this point is referred to as the shower-maximum.

1.2.2 Cherenkov Radiation

Cherenkov radiation is electromagnetic radiation emitted by a dielectric medium when a charged particle travels through it at a speed faster than the speed of light in the medium. The mechanism is commonly described as the analog of a sonic boom and the resulting shock wave front. Cherenkov radiation, when intense, appears as a bluish glow like that

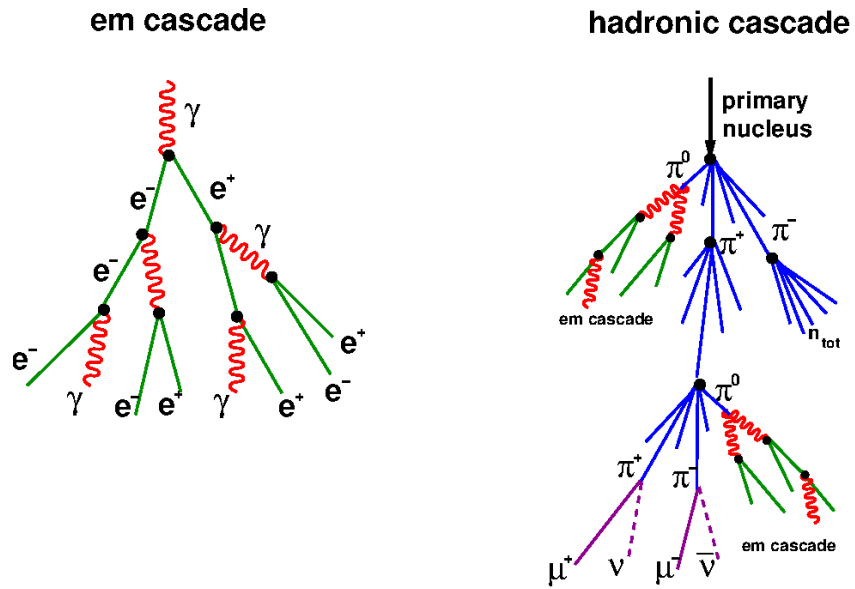


Figure 1.2: Processes involved in generating extensive air showers [11]. In an electromagnetic shower (left), there is only one kind of process involved, which corresponds to either pair production by a gamma-ray photon or radiation by an electron or positron. A hadronic cascade can have a number of other processes, including those involved in an electromagnetic shower, and this variety of ways in which the particles can lose momentum leads to a more dispersed set of photon showers.

noticed in the pools of water shielding some nuclear reactors. The phenomenon was experimentally studied by the Soviet physicist Pavel A. Cherenkov in 1934 [12] and was explained by Ilya M. Frank and Igor Y. Tamm in 1937 [13].

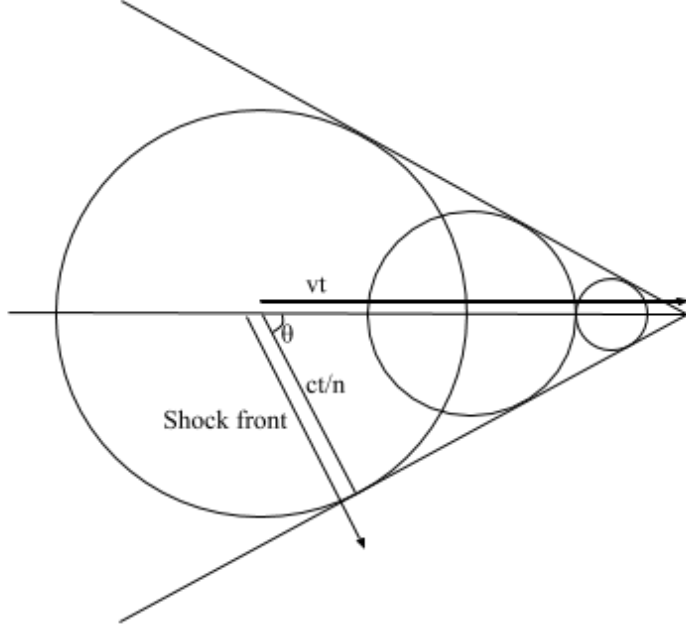


Figure 1.3: Mechanism of Cherenkov radiation where the horizontal line represents the charged particle moving through the medium, and the circles represent shock fronts from different points in the particle trajectory. These shock fronts can propagate only at c/n , but the particle moves through the medium at v which is larger.

The speed of light in a medium is given by c/n where n is the refractive index of light in the medium. When the speed of the particle exceeds this speed ($v > c/n$), a shock front appears between the region where an electric field due to the charged particle is present and one where it is not because the electric field can only propagate at the speed of light in the medium (c/n). The shock front travels at an angle given by

$\theta_C = \cos^{-1}(c/vn) = \cos^{-1}(1/\beta n)$ with radiation emitted in a cone with angle θ_C from the direction of propagation of the initiating charged particle as shown in Fig. 1.3. The number of photons per unit length of particle path per unit of wavelength is given by

$$\frac{d^2N}{dxd\lambda} = \frac{4\pi^2 z^2 e^2}{hc\lambda} \left(1 - \frac{1}{n^2 \beta^2}\right) = \frac{2\pi z^2}{\lambda^2} \alpha \sin^2 \theta_C \quad (1.1)$$

In Eqn. (1.1), N refers to the number of radiated photons, x is the length traveled through the medium, λ is the wavelength of the radiated photons, z the atomic number (the charge of the radiating particle). Finally, its uses the standard symbols for fundamental constants e the electron charge, α the fine structure constant, c the speed of light in vacuum, and h Planck's constant.

The equation has an inverse dependence on the wavelength means that more photons are radiated at lower wavelengths and so the radiated photons are mostly on the low-wavelength end of the spectrum. Since Cherenkov radiation is a coherent process, the electric field is perpendicular to the surface of the emission cone and the emission is completely polarized.

1.2.3 Imaging Atmospheric Cherenkov Telescopes

Imaging atmospheric Cherenkov telescopes (IACTs) detect the light produced in an extensive air shower (EAS) by the primary particle. EAS emit a cone of forward-beamed Cherenkov photons with a half-opening angle of $\sim 1^\circ$ [14]. This beam illuminates an elliptical region on the ground called the light pool which has an area of the order of 10^5 m^2 , with variations depending on the altitude of the shower maximum and inclination of the shower axis.

The Cherenkov technique resolves (in space and time) the shower development image captured by the telescope camera. This information is used to distinguish between different types of showers (hadronic vs γ -ray-initiated) by using the different spatial spread of the showers depending on initial particles. In particular, for VHE γ -ray showers, because the shower is compact in the transverse direction the direction of the ensuing shower is roughly along a cone with the thickness of the cone inversely dependent on the energy. For hadronic showers, the initial interactions lead to a less compact spread in direction of the resulting particles.

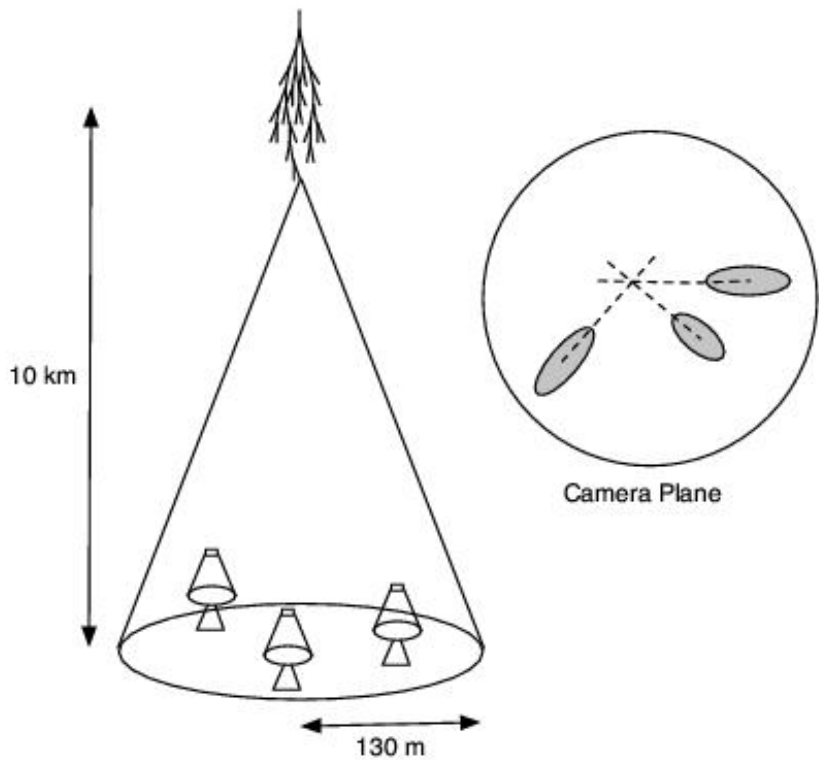


Figure 1.4: Illustration of an IACT array, with typical shower height and radius of light pool for γ -rays with primary energy > 100 GeV. Picture taken from [8].

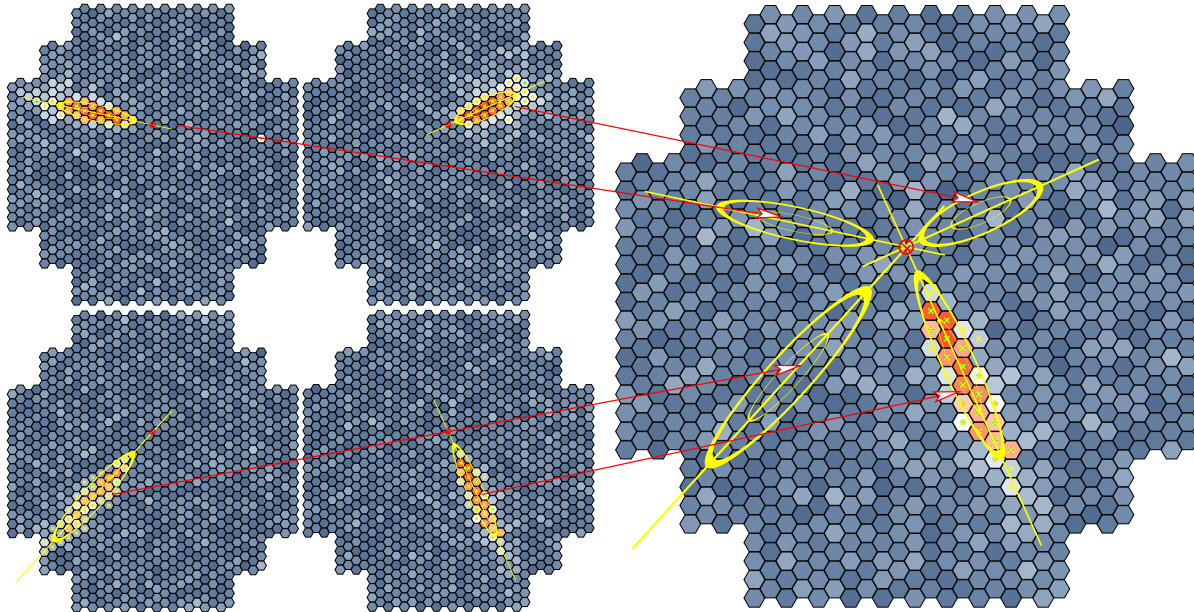


Figure 1.5: Gamma-ray induced air shower incident at a telescope array (left). Image of an air shower on the camera plane where each telescope image is characterized by an ellipse (right) [7]. The red lines indicate where each telescope image is reconstructed on the camera plane.

Modern IACTs use multiple telescopes operating in conjunction, which increases effective area as well as directional resolution. Combining the images from the different telescopes enables stereoscopic imaging allowing for reconstructing the axis of the air shower as shown in Fig. 1.4. The majority of EAS are generated by high energy cosmic rays, composed primarily of protons and nuclei, rather than gamma rays. The dominant interactions of these protons – nuclear hadronic interactions – are the same process commonly seen in particle colliders, producing showers dominated by high energy π mesons (π^0, π^\pm).

1.2.4 The VERITAS Instrument

The VERITAS instrument consists of four telescopes, each consisting of a reflector, a camera box, and a counterweight. The reflectors on each telescope are 12 m diameter

spherical Davies-Cotton mirrors [15]. The four telescopes are arranged in order to maximize collection area while being close enough for multiple telescopes to fall within the light pool for an air shower. Having multiple telescopes within the light pool allows for better stereoscopic reconstruction as demonstrated in Fig. 1.5. The distance between adjacent telescopes is ~ 100 m and the radius of the light pool for energies > 100 GeV is ~ 130 m.

Each VERITAS telescope uses 345 identical hexagonal spherical mirrors (of area 0.322 m^2 and radius-of-curvature of approximately 24m) giving a total reflector area of nearly 110 m^2 [8]. The hexagonal shape allows for more efficient packing of mirrors on the reflector surface.

The individual hexagonal mirrors need to be manually aligned so that the entire reflector will act as a single dish. The measure of the alignment of these mirrors is the point spread function (PSF), which describes the response of the detector to a point source at infinity. The better aligned the system, the smaller the value of the resulting PSF.

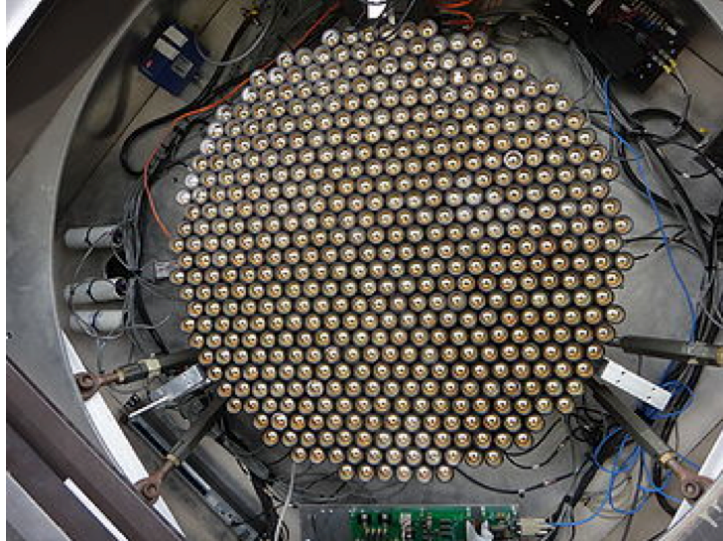


Figure 1.6: The PMT “pixels” in the VERITAS Camera. Picture taken from [16].

The camera in a VERITAS telescope is located at the focal plane of the telescope (12 meters from the mirrors) in a “focus box” of dimension 1.8m x 1.8m. The camera consists of 499 closed-packed circular photomultiplier tubes (PMTs, see Fig. 1.6), giving an angular

pixel spacing of 0.15 degree and a total field-of-view (FOV) of 3.5 degrees. The PMTs are arranged in a hexagonal pattern to maximize coverage.

At the low end of the VERITAS energy range, fluctuations in the night sky background (NSB) and (single) muons from cosmic-ray showers constitute a large fraction of the observed single-telescope events. VERITAS employs a three-tier trigger system to reduce the rate of these background events. The first trigger system works on the single-pixel level, the second checks for specific patterns of single level pixels within a timing window, and the third works at the array level, requiring simultaneous observations of an air-shower event in multiple telescopes (ensuring a "stereoscopic" view of the event). The three trigger levels are designated L1, L2 and L3.

The L1 trigger, which is the pixel-level trigger system, has constant fraction discriminators (CFDs) and threshold discriminators for each PMT in the telescope cameras. This trigger requires the signal from a PMT channel to be above a particular threshold, reducing contamination from the night sky background and electronic noise. This information is then passed on to the L2 trigger.

The L2 trigger, reduces effects from NSB and electronic noise by requiring correlations between adjacent pixels. Specifically, this trigger only triggers an output pulse when several adjacent pixels surpass the L1 discriminator threshold within some coincidence window (about 6 ns). The L3 trigger uses this to determine whether to store the data.

Relativistic muons in the atmosphere radiate Cherenkov radiation and comprise a large background source for Cherenkov telescopes at low energies. Muons decaying close to a telescope face produce rings in the camera, but these rings will only be large enough for detection by a single telescope. With this in mind, the L3 trigger is an array-level trigger which depends on receiving telescope level triggers from more than one telescope. Effective removal of the muon background allows sensitivity to the lower energy range where these backgrounds would otherwise dominate.

1.3 Shower Image Parameters

The shower image parameters are the input to the direction reconstruction that is the focus of this work. In any given telescope, the shower image is parameterized using various measurements including

- the image axis – defined as the line minimizing the signal-weighted sum of squares of perpendicular distance between triggering pixels (see Fig. 1.7).
- the time gradient – a measure of the difference in time of arrival, along the image axis, of the signal at a pixel .
- the length of the image (see Fig. 1.8) – the r.m.s spread of the signal-weighted triggered pixels parallel to the image axis [17].
- the width of the image (see Fig. 1.8) – the r.m.s spread of the signal-weighted triggered pixels perpendicular to the image axis. The length and width together provide the major and minor axis of an ellipse containing the majority of the signal, and are referred to as the Hillas parameters and the Hillas ellipse.

A number of other parameters are used in the complete reconstruction of the shower, but these are the most relevant to the direction reconstruction, and specifically to the direction reconstruction process using the boosted decision tree (BDT) angular reconstruction.

1.3.1 The *Disp* Parameter

The *Disp* parameter is a measure of the displacement between the center of the Hillas ellipse (the center of gravity of a shower image at a telescope), and the origin of the shower in the camera plane (Fig. 1.9). This is a telescope-level parameter with a head-tail ambiguity, but with multiple telescope images, it can be used in estimating the direction of

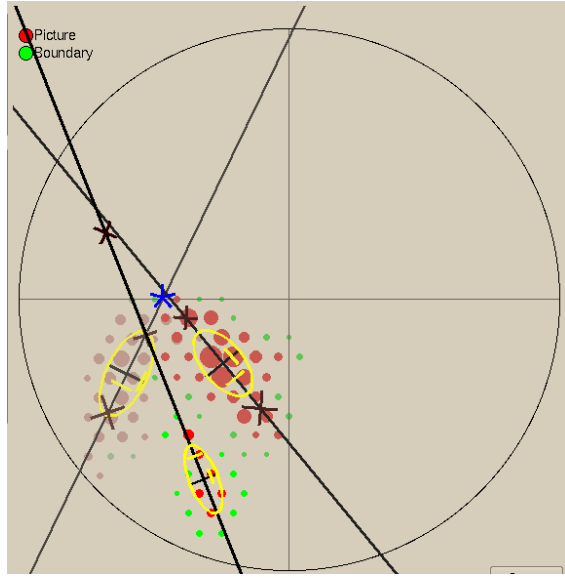


Figure 1.7: The image axis parameter is the line of best fit for the shower image on a single telescope. This best fit is measured by minimizing the signal-weighted sum of squares of residuals. Picture taken from [8].

the initiating gamma ray. This is based on the idea described in method (c) of Hofmann[18].

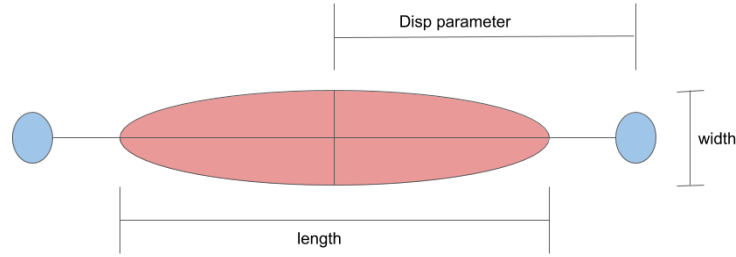


Figure 1.8: Hillas Ellipse (red), with the major axes and the estimated or calculated location of the origin of the shower in the camera plane (blue).

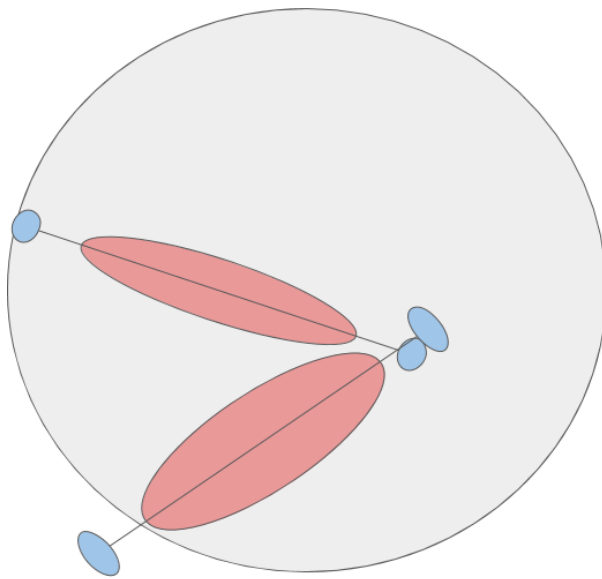


Figure 1.9: The Hillas ellipses (see Fig. 1.8), as used to reconstruct shower direction. In a single telescope image, there is an ambiguity in the direction of the displacement from the center of gravity of the image. However, in a multi-telescope array this ambiguity can be resolved by looking at several Hillas ellipses in conjunction and minimizing the location of the shower source.

Chapter 2

Simulation and Analysis Packages

2.1 Overview

A large number of charged cosmic ray events are included among the triggering events despite the three-level trigger. Most current generation experiments use analysis techniques based on Hillas parameters [17], using the second moments of the distribution of pixel signal amplitudes, which for VERITAS, yield an angular resolution of $\sim < 0.1^\circ$ at 1 TeV. However, significantly more information can be extracted from the recorded data using a template library containing expected shower images for a given set of shower parameters. This template library can then be compared to the recorded images for any given event and the best-fit shower parameters can be determined resulting in improved resolution in direction and energy reconstruction. This section provides a brief overview of the Monte-Carlo simulations used to generate these templates for VERITAS.

2.2 Shower Generation

This section describes the prediction of the expected Cherenkov light distribution in the camera focal plane for a given set of primary particle parameters. The production of mean shower images is divided into two steps: the generation of large Monte Carlo datasets of air showers and the simulation of the detector response. The electromagnetic air showers in the atmosphere are simulated with the CORSIKA (COsmic Ray SImulations for KAscade) [19] program and simulations are performed over a range of parameters like energy, zenith angle and impact distance.

In the simulation, which contains the shower generation from section 1.2.1, when a charged particle exceeds $v > c/n$, Cherenkov photons are generated. The number of photons emitted is calculated for a given extent of the path and the propagation directions are randomly selected from the surface of a Cherenkov cone (i.e. $\theta_c = \cos^{-1} \beta/n$). Each photon is then tracked through the atmosphere until it reaches the altitude of the observatory. CORSIKA does not track whether the photon hits a telescope reflector, but instead defines a volume around each telescope in order to filter photons to store. Photons whose trajectories do not intersect this volume are not stored.

With the instrument pointing at the shower source, each of the telescope cameras lies on a plane perpendicular to the shower axis, making the shower projection plane and the camera planes parallel. The CORSIKA simulation output contains the photon distribution at the telescope altitude, and the arrival direction of each photon. For each event, the Cherenkov photons falling onto the mirror elements are tracked by their arrival times, initial direction, and wavelength. The detector response is modeled using the atmospheric density profile, optical absorption and some of the detector characteristics such as its light-collecting area, and phototube quantum efficiency. It also accounts for the physical structure of the telescopes such as occultation by the quadrupod arms and the camera box. The images are produced for the VERITAS telescopes which use a Davies-Cotton design

for the reflectors and cameras with 499 pixels, each pixel having a field of view (FOV) of 0.15° in diameter [9].

The shower images are generated for a range of first-interaction depths, energies, wobble offsets (when the pointing is offset from the target object) and impact distances. A multidimensional interpolation algorithm is used to interpolate between the templates, allowing production of an image template for any shower parameters within the parameter ranges. An additional parameter included here is the effect of the geomagnetic field on the electromagnetic showers [20]. Once the full set of templates has been created, they can be compared with the observed images by performing a global fit to the telescope image data using a model for the expected pixel (PMT) amplitudes. Shower parameters are determined by maximizing an array likelihood function, as outlined in [21].

2.3 The VEGAS Analysis Package

The VERITAS observation and simulation data contain the PMT pulses, pointing direction, time and time gradient (which are extracted from the PMT pulses), and other trigger and operational conditions. To produce a sky map, these data files are piped through a series of functions to extract, among other things, energy and direction information. At VERITAS there are two standard analysis packages for this process (*VEGAS* [22] and *EventDisplay*[23]), both based in ROOT [24] within C++, with a similar set of functions. While the analysis methods in this work can be and are applied in both analysis packages, the analysis in this work was performed using the *VEGAS* package. *VEGAS* consists of 6 distinct processes, initially written as 6 distinct modules, as follows:

- Stage 1: Calibration Calculation – This stage calculates the hardware dependent parameters of the VERITAS data and collects relevant information at each trigger level (pixel, telescope, and array) to determine a set of calibration parameters. The

following stages can then use these parameters in conjunction with the data to remove any hardware dependence.

- Stage 2: Calibration Application – This stage calculates calibrated charge information for PMT traces using information on pedestals, relative gains, and relative channel timing. In more recent iterations, the analysis module for stage 2 also performs the functions previously performed in stage 3.
- Stage 3: Image Parameterization – This stage removes noisy pixels using stage 1 & 2 information and calculates the image parameters (described in section 1.3). This stage treats each telescope independently and so image parameters are calculated for each telescope image.
- **Stage 4: Shower Reconstruction** – This is the most important stage for the purposes of this work. This stage performs an array-level reconstruction of the shower, using individual telescope information to calculate **shower direction** (the original arrival direction of the candidate photon), event energy, depth of the shower maximum, and core location.
- Stage 5: Event Selection – This stage is designed to apply cuts to events based on the output of the previous stages to better distinguish hadronic showers from gamma-ray showers, as well as enforce any other restrictions on telescope-image or stereoscopic parameters.
- Stage 6: Results Extraction – This stage calculates and displays the final results of the desired analysis – single telescope analysis, stereoscopic analysis, spectral analysis or temporal flux analysis.

The focus of this work will be on the direction reconstruction part of stage 4.

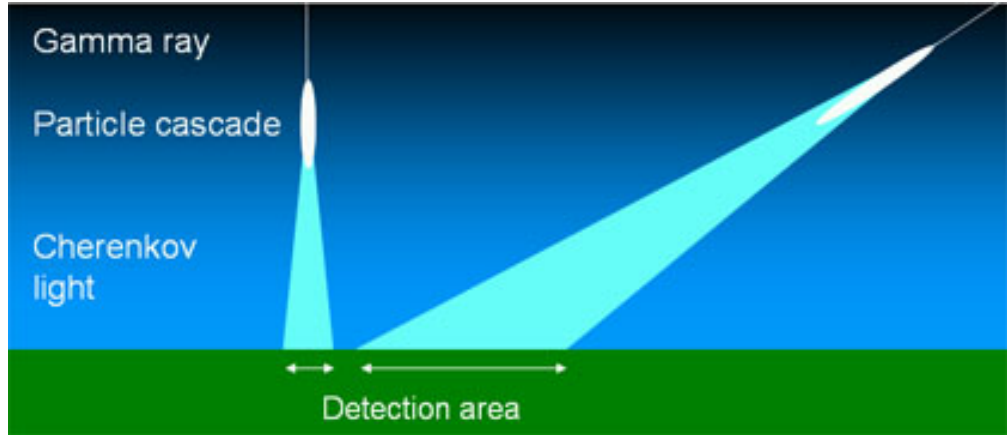
2.4 Direction Reconstruction

The standard method (henceforth Method0) of shower direction reconstruction is based on the intersections of the major axes of Hillas ellipses (see Fig. 1.8). This method carries a lot of stereoscopic information and is in general very powerful. However, for large zenith angles (LZA), one expects shower images (and therefore Hillas ellipses) in the camera plane to be from the same region in the lightpool (see Fig. 2.1) and close to parallel, so that small uncertainties in major axis determination result in large uncertainties in the fiducial location of the reconstructed gamma ray in the camera plane (the “shower location”). As shown in Fig. 2.2, for lower energies and at larger zenith angles, there is a substantial degradation in angular resolution.

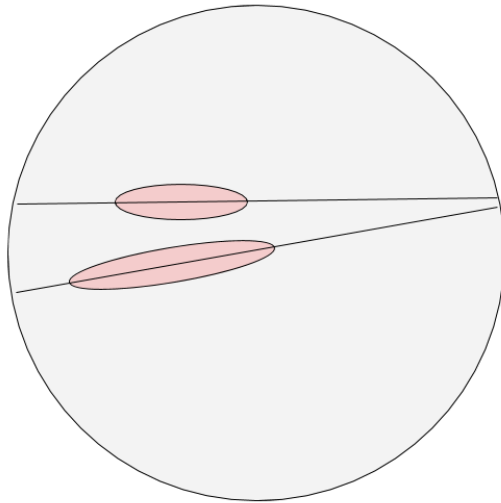
2.4.1 The *Disp* Method

To compensate for this loss of predictive power, the *Disp method*, calculates the *Disp* parameter (quasi-analytically, using lookup tables and interpolating, or using **boosted decision trees**) for each individual telescope image to determine two potential locations for the arrival direction – along the major axis on either side of the weighted centroid of the image (see Fig. 1.8). This parameter is the (angular) vector displacement between the weighted centroid of the shower image and the estimated arrival direction of the initiating photon. In addition, the method also determines the two-dimensional uncertainty on this parameter which is expressed in terms of the radial (*DispError*) and angular (*MAError*) uncertainties. Together, these three parameters fully specify the direction of the initiating photon and the uncertainty on it, up to the head-tail ambiguity.

The method then compares this pair of coordinates (one at the head, and one at the tail) for each pair of telescopes in the event reconstruction to find the pair of coordinates, one from either telescope, that are closest to each other (see Fig 2.3 for visual explanation).



(a) The light pool for Cherenkov showers at small zenith angle versus at large zenith angle. Picture taken from [7].



(b) The Hillas ellipses resulting from two telescopes at LZA.

Figure 2.1: The stereoscopic method is less effective at large zenith angles due to the lightpool from these events being much larger than the coverage of the telescopes. This results in the telescopes being in the same region of the light pool and therefore nearly parallel Hillas ellipses. In such cases, the stereoscopic method of reconstruction will have a large uncertainty in the point of intersection of these two axis, which corresponds to a large uncertainty in the reconstructed direction.

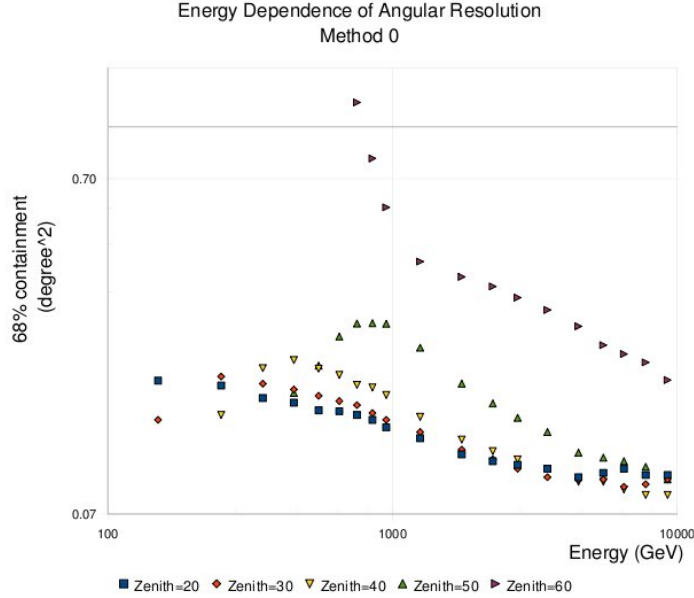


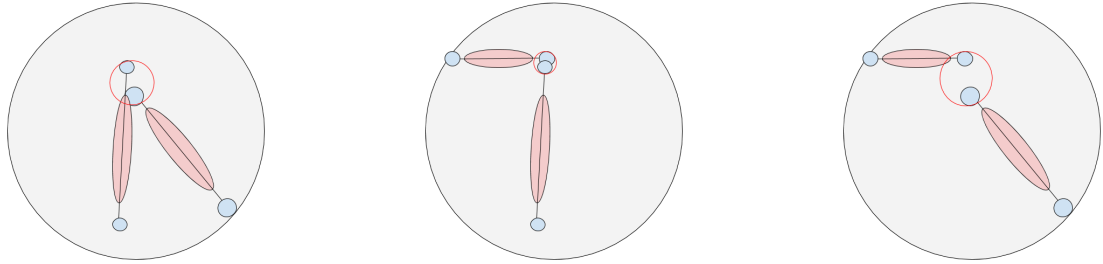
Figure 2.2: Angular resolution of Method0 direction reconstruction as a function of energy scale and zenith angle. From [8].

The weighted mean of this pair of coordinates is taken as the reconstructed shower direction, with the weights given by *DispError* and *MAError*. The root mean squared (RMS) distance of the two closest points (the points in the red circle in Fig. 2.3(d)) is taken to be the uncertainty on this position.

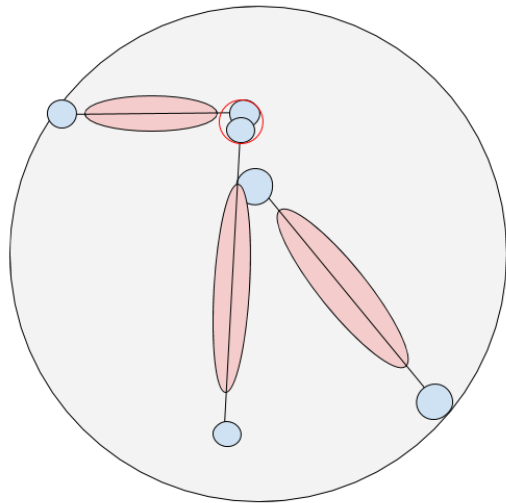
While using a quasi-analytic lookup table already provides substantial improvements on the LZA performance of the direction reconstruction, using boosted decision trees (BDTs) provides significantly better resolution comparable to (and in some regimes better than) that from the geometric reconstruction in the medium zenith angle range ($40^\circ - 50^\circ$).

2.5 Boosted Decision Trees

Decision trees use a predictive model, which maps parameters for an event to the value of the *Disp* parameter for the event. For example, Fig. 2.4 shows a decision tree that uses



(a) First pair of telescopes in recon- (b) Second pair of telescopes in re- (c) Third pair of telescopes in
struction, with the pair of closest construction, with the pair of clos- construction, with the pair of clos-
coordinates. est coordinates. est coordinates.



(d) All telescopes in reconstruction, with the pair of closest co-
ordinates from *all* pairs of telescopes.

Figure 2.3: Iterating through the unique pairs of telescopes, the closest coordinate pair is chosen, and the mean of those coordinates is taken as the direction of the initiating particle.

observed quantities to determine the temperature outside. The tree starts at the “root node”, which is the first test or question posed on the input data. The answer to this test determines the “branch” of the tree that is followed (in Fig. 2.4, Sunny or Overcast). Branches lead to “nodes,” which can either terminate (“leaf-nodes”), providing an answer, or pose a question and branch out again (“non-leaf nodes”) as demonstrated in Fig. 2.4.

The questions asked at each point are determined from a predictive model which may be based on analytic calculations (as in this example), or on Monte Carlo simulations (as in the case of this work). A basic algorithm for boosted decision tree (BDT) learning takes an input sample of data, generates a decision tree, uses a boosting algorithm to better discriminate mis-modeled inputs, and runs tests to provide some measures of its own performance. BDTs are especially robust for variables with non-linear correlations and have a fast application to data, relative to some other algorithms. This section contains a brief description of these individual steps.

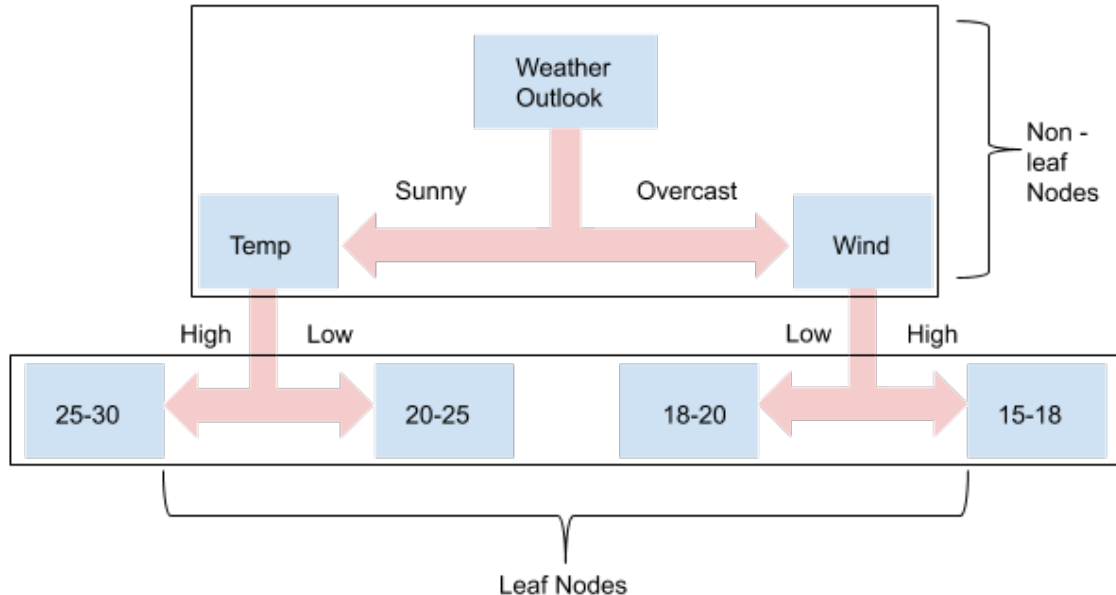


Figure 2.4: An example of a BDT to determine the temperature using observables. Each test or question is represented by a “node,” which creates two or more “branches” of the tree. Each of these branches represent a particular answer (or set of answers) to the test/question. The final results, where no test is performed is referred to as a leaf.

2.5.1 Training

Decision trees are a type of supervised learning algorithm. This means the training data contains the input variables as well as the expected output variables. For our purposes, this means the algorithm is provided with a training sample comprised of the values of the parameters used for the reconstruction of each event along with the true value (from simulations) of the parameter to be reconstructed. The training process then generates correlation matrices for the dependent variables. With this information the algorithm is able to create a decision tree where each non-leaf node denotes a test on an attribute and each branch represents an outcome of the test, at each step using a test that best bifurcates the input data. In Fig. 2.4 this can be represented by the fact that on an overcast day, the wind-speed is a strong discriminating factor, but on a sunny day wind is a smaller effect.

2.5.2 Boosting

To avoid having multiple identical trees, a higher weight is assigned to events that are canonically hard to discriminate. This means that within the training, more time is spent on discriminating between events that are hard to distinguish and this assigning of weights to preferentially train more on specific parts of parameter space is referred to as boosting.

2.5.3 Testing

The implementation of the *Disp* method in *VEGAS* (and *EventDisplay*) uses the ROOT Toolkit for Multi-Variate Analysis (TMVA) package. The TMVA package contains implementations of several complex algorithms including neural networks, Fisher discriminants and BDTs. The TMVA package contains a built-in testing step to measure certain parameters to help determine the goodness of the training. This step is used to measure deviations of the reconstruction of the testing data-set and the training data-set.

A large difference between the performance on the training and testing sets could mean the method has been trained on noise in the training data-set rather than on relevant parameters. This misinterpretation of nuisance parameters or noise in the training sample as relevant effects is referred to as *overtraining*.

2.6 Noise in Simulations

The NSB level is also a priori expected to influence the reconstruction efficiency for gamma rays. A higher level of NSB photons increases the threshold needed to remove background photons, thereby causing a greater loss of lower energy gamma rays. On the other hand, NSB photons may “promote” sub-threshold showers over our trigger threshold. Given these competing effects, it is expected that the NSB needs to be modeled in our simulations.

To incorporate this effect in the simulations, gamma-ray shower simulations are created with multiple different noise levels. For the purposes of this work, simulations with noise levels of 200, 250, 300, 350, and 450 MHz were used.

While the units used for noise in this work are MHz, this frequency is not that of the background photons. Instead this represents the photon flux (which is measured in photo-electrons $\text{ns}^{-1} \text{ m}^{-2} \text{ sr}^{-1}$) folded in with a number of instrument parameters that include mirror area (m^2), reflectivity (as %) and pixel size of the PMTs (rad). It tracks roughly the number of photo-electrons from the night-sky background per pixel of the camera. This range of values should accurately recreate the NSB levels at VERITAS observations.

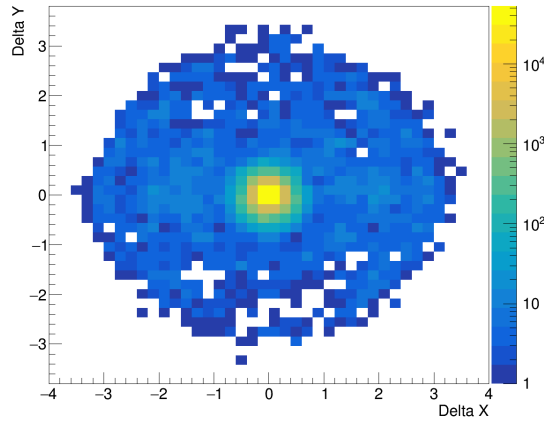
Chapter 3

Analysis Methods

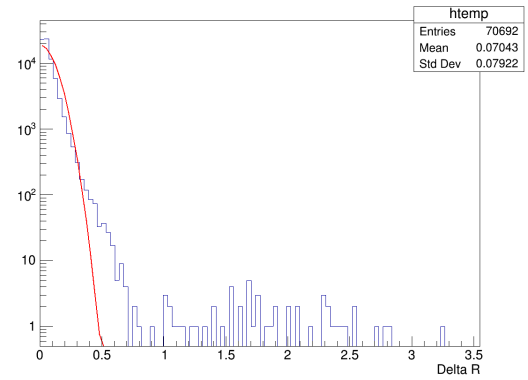
3.1 Preliminary Test and Motivation

The motivation for this work was to understand, refine, and document the *Disp* method of direction reconstruction. This method was expected to be useful to better resolve objects observed close to the horizon and facilitate studying the stability of the reconstruction to the zenith angle of observation. There was also the possibility of using machine learning algorithms to improve resolution beyond that of the standard geometric reconstruction. In particular, an improved angular resolution on the Crab may open up the possibility of resolving the spatial extent of the Crab Nebula with the VERITAS instrument.

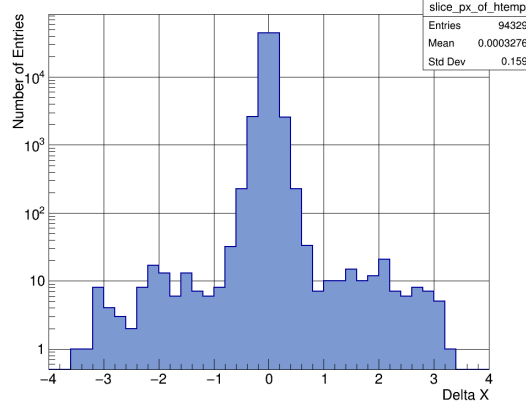
For the purposes of this work, the 68% containment radius in angular position (R_{68}) is used as a measure of angular resolution and performance of the reconstruction. This was measured in two ways - one numerically and one using a 2D Gaussian fit to the deviation of the reconstruction. From here (see Fig. 3.1) it was clear that the Gaussian fit was not an accurate representation of the underlying data, but could nevertheless provide some insight into it.



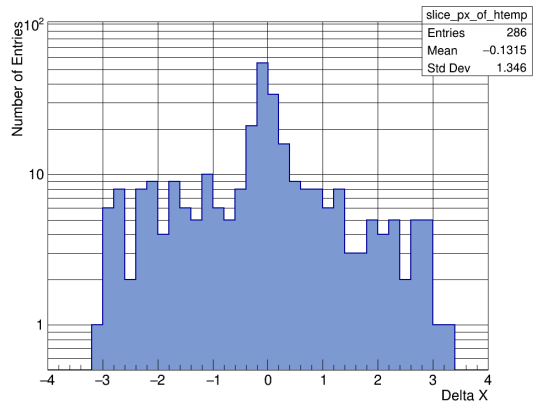
(a) A histogram of the 2D projection of the angular deviation of the reconstructed direction. The colors denote the number of entries in a given bin.



(b) The radial deviation of the reconstructed direction for a diagonal slice of the 2D histogram where $\Delta Y \in \Delta X + (-0.05, 0.05)$.



(c) The distribution (in ΔX) of the reconstructed direction for a horizontal slice of the 2D histogram where $\Delta Y \in (0.0, 0.2)$. There is a clear central Gaussian shape in the central 1° region of the plot, in addition to a shorter, wider Gaussian with amplitude $\sim 10^{-3}$ times that of the central Gaussian.



(d) The distribution (in ΔX) of the reconstructed direction for a horizontal slice of the 2D histogram where $\Delta Y \in (0.8, 1.0)$.

Figure 3.1: Reconstruction of the simulation direction using the *Disp* Method for simulations at 45° zenith angle with $10^3 \text{ GeV} < E < 10^{3.5} \text{ GeV}$. From (b) it is evident that a R_{68} based on the width of the best-fit Gaussian would not be an accurate measure of the R_{68} , and would consistently overestimate the resolving power of the method. However, it is also clear that the vast majority of statistics fall in the central region, and that the width of this region can provide a first-order approximation to the R_{68} .

Based on the distribution of the deviation of reconstructed direction of the simulations (Fig. 3.1) from the simulated direction, it was determined that a fit to the central Gaussian could provide some useful information about the R_{68} , and to this end, the 2D distribution (Fig. 3.1(a)) was fit with the superposition of two Gaussians, with the 68% of this superposition as a first-order approximation to the R_{68} . Additionally, it was determined that a numerical integral would provide a more accurate measure of this quantity and so the distribution of radial deviations was integrated from the tail inwards, until 32% of the events were counted and this value of the radial deviation from the simulated direction was used as a more accurate measure of the R_{68} ; a representative sample of the results is shown in Fig. 3.2.

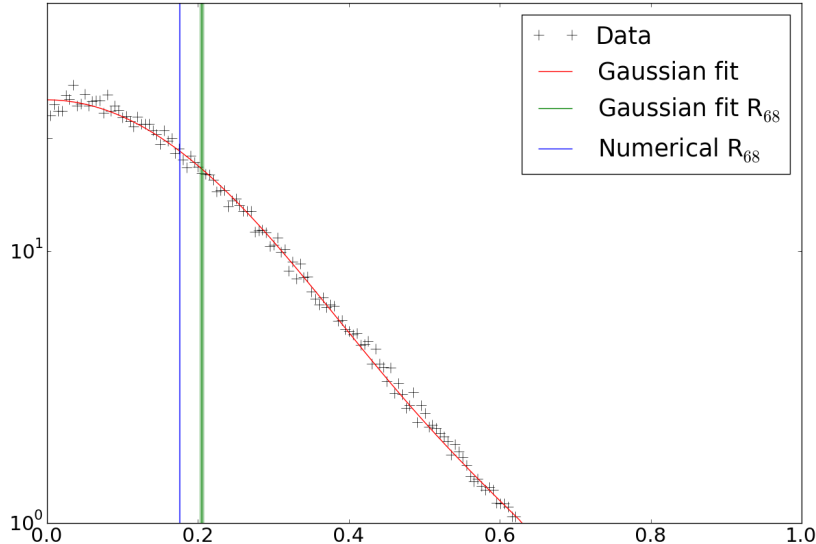


Figure 3.2: The R_{68} calculated for a simulation using a fit to a superposition of two Gaussians (green vertical line) and a numerical integration from 1° inwards (blue vertical line), overlaid on a radial slice for Monte-Carlo simulations.

A preliminary test for the R_{68} of the data was enabled by a set of runs where the Crab was tracked from horizon to culmination and back to the horizon (from the nights of Jan. 12 2018, Jan. 13 2018, and Jan. 04, 2019). This provided a reference data set with high

significance to track the energy and zenith dependences of the direction reconstruction in stable (and therefore directly comparable) weather conditions. The differential resolution for the Crab data was measured in several energy and zenith bins and is presented in Fig. 3.3.

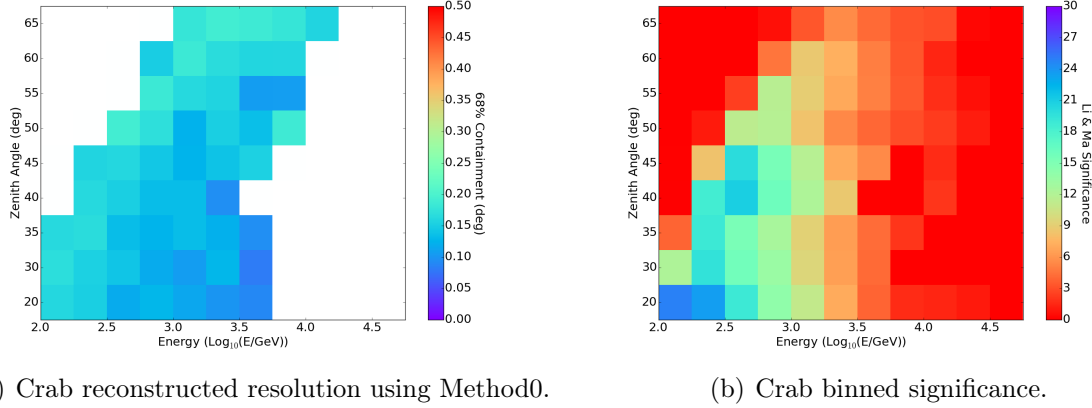


Figure 3.3: Reconstruction of the Crab direction using Method0 (standard geometric reconstruction from *VEGAS*). On the left, the regions of white denote regions where Li & Ma significance $< 3\sigma$ (for a description of this, see section 3.3.1).

3.2 *Disp* Table and R_{68} Dependencies

The BDT weight tables were generated independently of the old *Disp* method in order to have well-understood documentation of the underlying effects and dependencies.

3.2.1 Zenith Angle Dependence

A set of *Disp* tables was generated with a small sample of simulated events ($n \approx 1.9 \times 10^6$) across the range of zenith angles of interest ($20^\circ - 65^\circ$). This was compared to the regular *Disp* method. Since there was no record of the training sample size for the standard tables, this test sample was useful in determining the resolution of the *Disp* method with a

relatively small computational footprint. Additionally, it allowed for some simple tests of dependence of the *Disp* tables on parameters not explicitly in the *Disp* tables.

These small *Disp* tables and the standard *Disp* tables were used to reconstruct simulation events and compared with Method0 (the standard method of direction reconstruction). In both cases, the *Disp* method performs better than Method0 at the largest zenith angles ($\geq 55^\circ$, see Fig. 3.4-3.5 for R_{68} of the *Disp* methods divided by that for Method0 at the same zenith angle).

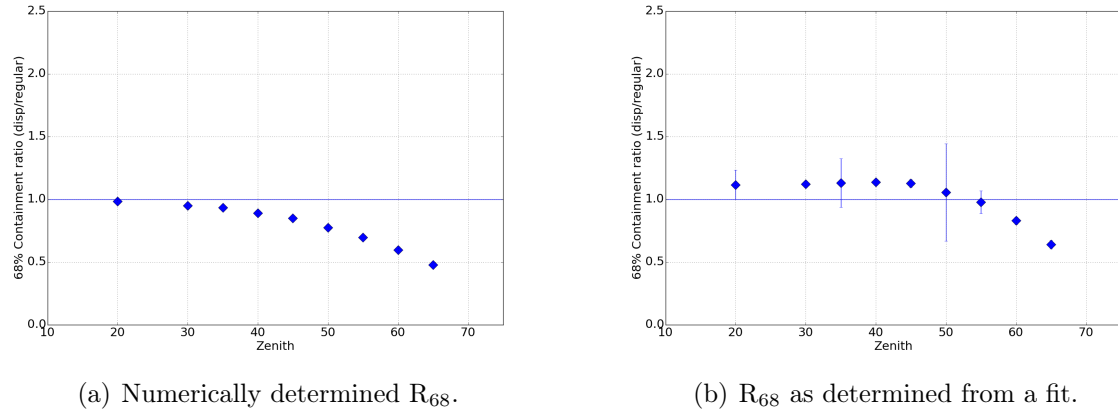
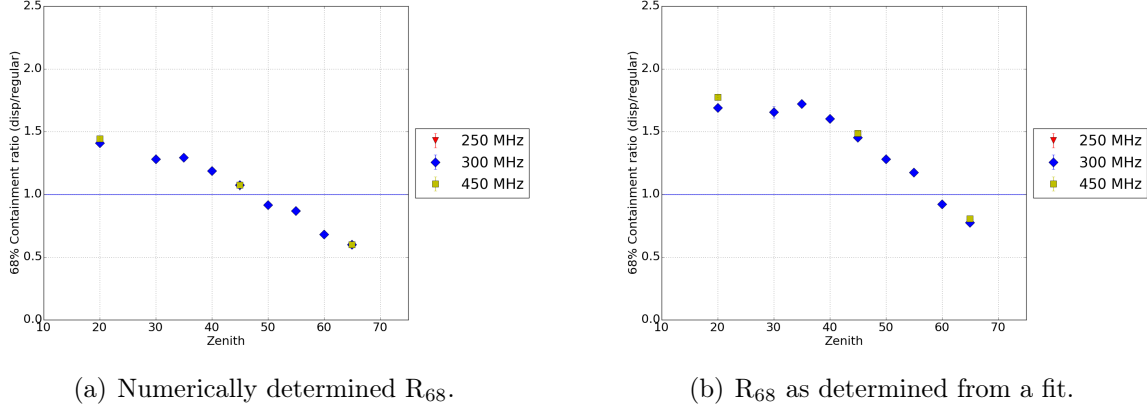


Figure 3.4: Ratio of R_{68} of the “standard” *Disp* table to that from Method0, with the numerically determined R_{68} (left) and that found from the fit to two Gaussians (right). Since this is the ratio of methods, the horizontal blue line denotes the performance using Method0; and the *Disp* method definitely performs better than Method0 for zenith $\gtrsim 50^\circ$. The large uncertainties in some of the fit values arise from the non-Gaussian shape of the overall distribution, and the long tails causing a poor fit to the superposition of two gaussians.

From Fig. 3.4, we can see that the *Disp* method outperforms the standard method across zenith angles when using the numerical integration, i.e. the tails of the distribution from the geometric method are better behaved than those found using the *Disp* method. However, when using the 2-Gaussian fit, which provides an understanding of the central region where most events lie, the *Disp* method outperforms the geometric reconstruction only in the LZA range ($\phi \gtrsim 50$). This is considered the regime of interest for the *Disp*

method.



(a) Numerically determined R_{68} .

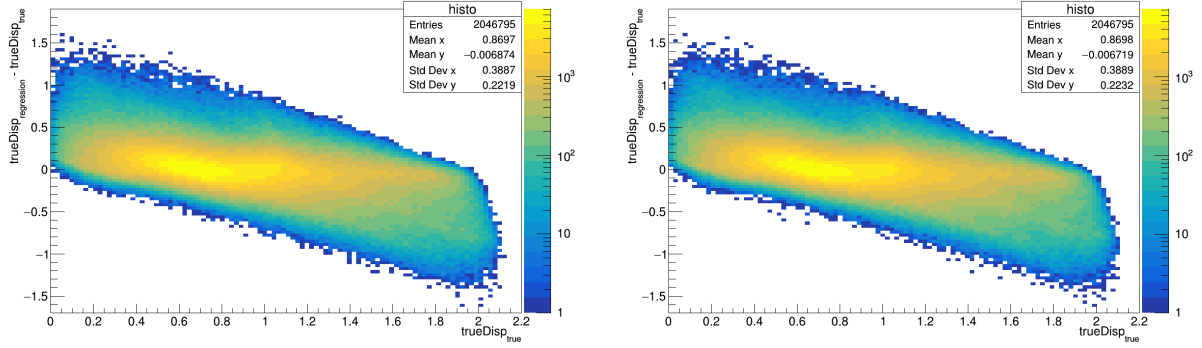
(b) R_{68} as determined from a fit.

Figure 3.5: Ratio of the R_{68} from reconstruction using the small *Disp* table ($\sim 1.9 \times 10^6$ events all at noise = 250 MHz) and that from Method0 with the numerically determined R_{68} (left) and that found from the fit to two Gaussians (right). Note the horizontal blue line denotes the performance using Method0, so this method performs better than Method0 for zenith $\gtrsim 50^\circ$.

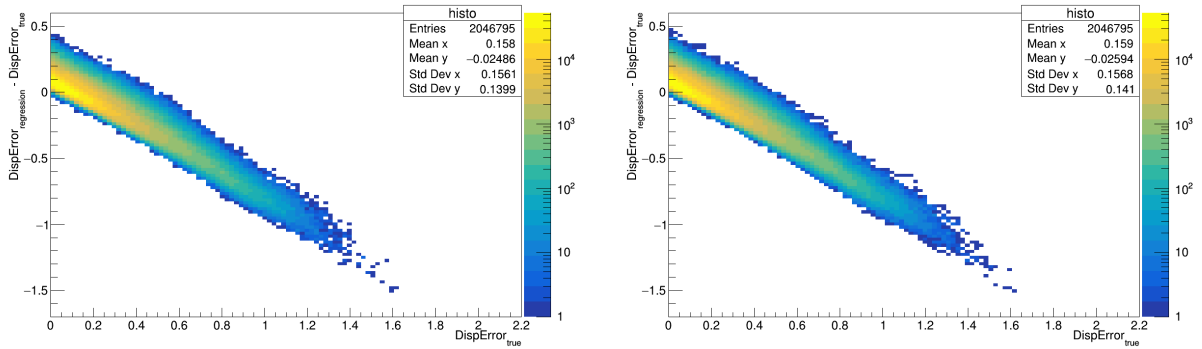
3.2.2 Over-training

BDT-based regression is quite robust under non-linear correlations between discriminating parameters. The primary vulnerability of this method is that to over-training - where the decision tree starts to be informed by noise and nuisance parameters in the training sample rather than relevant effects. This results in substantially different reconstruction efficiencies between training and testing samples. The ROOT TMVA package includes a test for over-training where it randomly selects a given fraction of the supplied events (for the purposes of this work, this fraction was taken to be 50%) to use for testing. These events are then not used to train the regression trees and are instead used only to generate a measure of the over-training. This check of the over-training for one of the test tables (noise = 450 MHz), shown in Fig. 3.6, demonstrates that there was no significant over-training of the table, at least based on effects present only in the training sample.

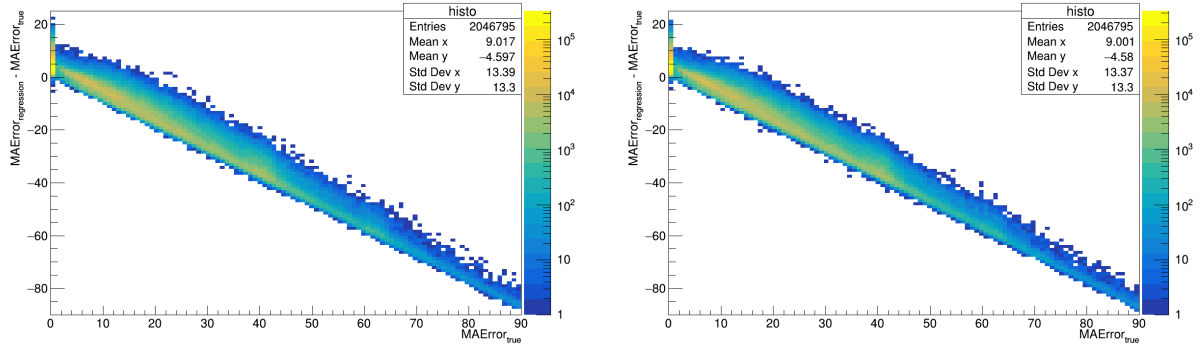
There remains however, the possibility of effects related to noise level that might appear in the training *and* testing samples (which are generated separately at each noise level), but not in observational data sets, which would be overlooked by this measure of over-training.



(a) Deviation of reconstructed $Disp$ parameter from Monte-Carlo $Disp$ parameter in training sample. (b) Deviation of reconstructed $Disp$ parameter from Monte-Carlo $Disp$ parameter in testing sample.



(c) Deviation of reconstructed $Disp$ Error parameter from Monte-Carlo $Disp$ Error parameter in training sample. (d) Deviation of reconstructed $Disp$ Error parameter from Monte-Carlo $Disp$ Error parameter in testing sample.



(e) Deviation of reconstructed $MAError$ parameter from Monte-Carlo $MAError$ parameter in training sample. (f) Deviation of reconstructed $MAError$ parameter from Monte-Carlo $MAError$ parameter in testing sample.

Figure 3.6: Over-training check on reconstruction using a $Disp$ table generated at a single noise level. The left column shows the deviation of the reconstructed parameter from the true value in the training sample and the column on the right shows the same in the testing sample. The difference between the two columns is small which suggests there is little or no overtraining.

3.2.3 Noise Related Effects

The first set of *Disp* tables was also generated at a single noise level (250 MHz), allowing us to test the dependence of the resolution of this method (as measured by R_{68}) on noise level in the testing sample – some kind of noise-dependent effect would suggest over-training that would not be evident from the testing sample in the ROOT TMVA method since all the data provided to the package would have been at the same noise level. A comparison of angular resolution across noise levels revealed no significant dependence of the R_{68} on noise (see Figs. 3.4, 3.5 and 3.7).

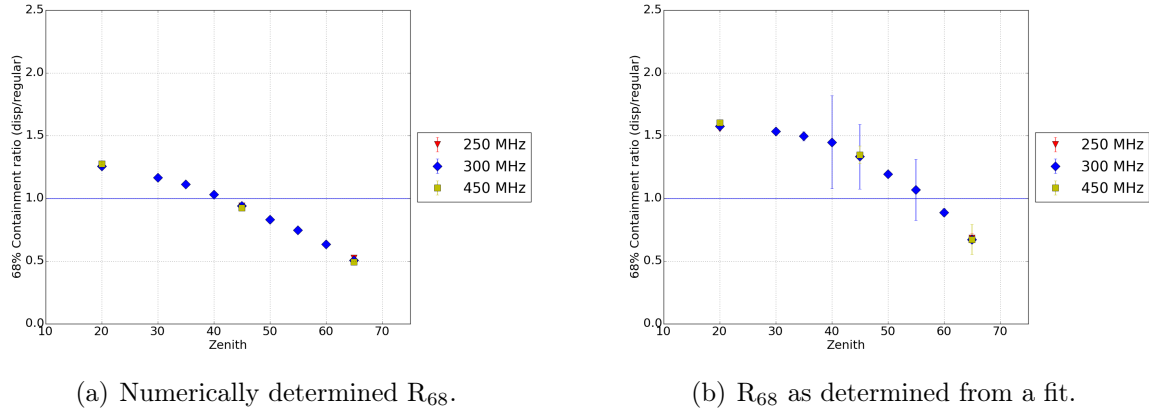


Figure 3.7: Ratio of R_{68} of the noise=450MHz *Disp* table ($\sim 2.1 \times 10^6$ events) to that from Method0 with the numerically determined R_{68} (left) and that found from the fit to two Gaussians (right). Note that the result is largely independent of the noise level in the simulation sample being reconstructed. The large uncertainties in some of the fit values arise from the non-Gaussian shape of the overall distribution, and the long tails causing a poor fit to the superposition of two gaussians.

A second set of test *Disp* tables was generated using a single noise level (noise = 450 MHz) to test for over-training related to noise in the training sample (see Fig. 3.7). These tables performed slightly better than the first test tables and comparably to the standard *Disp* tables, but not significantly so. Since the noise-related effects did not seem to play a significant role in reconstruction, noise was dropped as a discriminating parameter for further analysis. Together, these two tests confirm that we do not expect the *Disp* method

reconstruction to be dependent on the noise levels in either the training sample or the data being reconstructed and therefore this reconstruction should not be sensitive to different NSB models.

To generate a set of *Disp* tables with better angular resolution (as measured by R_{68}), another set of *Disp* tables was trained on a larger number of simulations across zenith angles (as before) as well as across the noise spectrum. Since noise was determined not to impact the reconstruction, the events at different noise levels were used only to create samples with greater statistics.

3.2.4 Higher Statistics Tables

Once it was determined that there was no significant over-training in the small sample *Disp* tables, and the noise level had little bearing on the R_{68} measure of the reconstruction, it was determined that different noise level simulation events could be used as independent training events to have a higher statistics *Disp* table, and make small improvements on the statistical uncertainty on the reconstruction. The simulation data from across the noise spectrum and zenith range was used to generate a *Disp* table that sampled the entire parameter space more exhaustively.

A new set of *Disp* tables was generated (Fig. 3.8) with a training sample four times that of the initial test tables. The improvements in resolution due to change in sample size were modest, and confined to the range of zenith angles ($\phi < 45^\circ$) where the standard method outperforms the *Disp* method quite considerably.

As expected from the small statistical uncertainty on the R_{68} values, this increase in sample size did not lead to any meaningful improvements and a training sample of $\sim 2 \times 10^6$ was determined to be sufficient to achieve the desired resolution with small uncertainties.

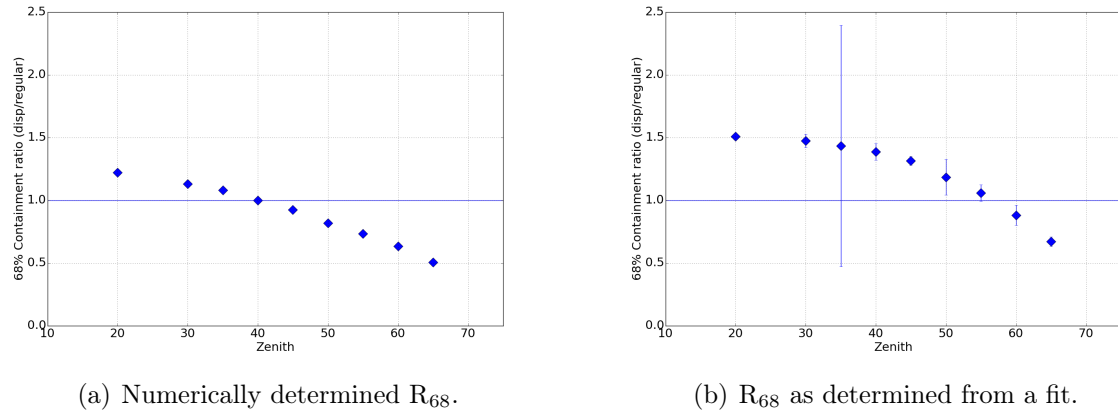


Figure 3.8: Ratio of R_{68} of the noise=450MHz *Disp* table ($\sim 8.4 \times 10^6$ events) to that from Method0 for a higher statistics *Disp* table with the numerically determined R_{68} (left) and that found from the fit to two Gaussians (right). The large uncertainties in some of the fit values arise from the non-Gaussian shape of the overall distribution, and the long tails causing a poor fit to the superposition of two gaussians.

3.2.5 Acceptance Correction for Offset from Camera Center

Showers arriving further from the camera center have a larger fraction of the shower arriving outside of the camera and therefore being lost. These showers are therefore reconstructed with a lower efficiency and resolution than showers arriving closer to the camera center. To compensate for this in the BDT training, so that the training sample does not mis-characterize the overabundance of events closer to the camera center as an anisotropy in incoming gamma rays, we fold in an acceptance correction by assigning a larger weight to events that are further away from the camera center.

The acceptance correction used here, i.e. the weight assigned to each event as a function of distance from the camera center, affects the training sample and therefore might be assumed to affect the resolution in a zenith dependent way, perhaps explaining the difference in performance between the new *Disp* tables and the old ones. This was tested by using a number of different correction functions in the training sample, which are shown in Fig. 3.9

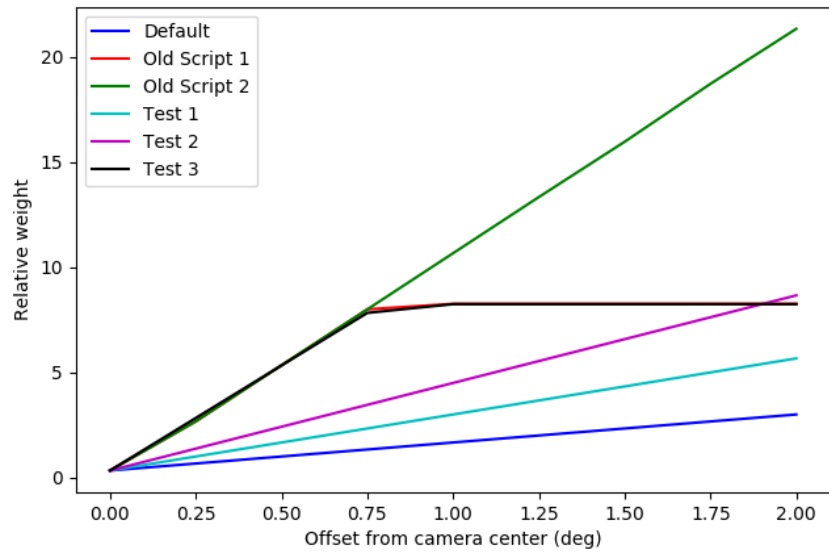
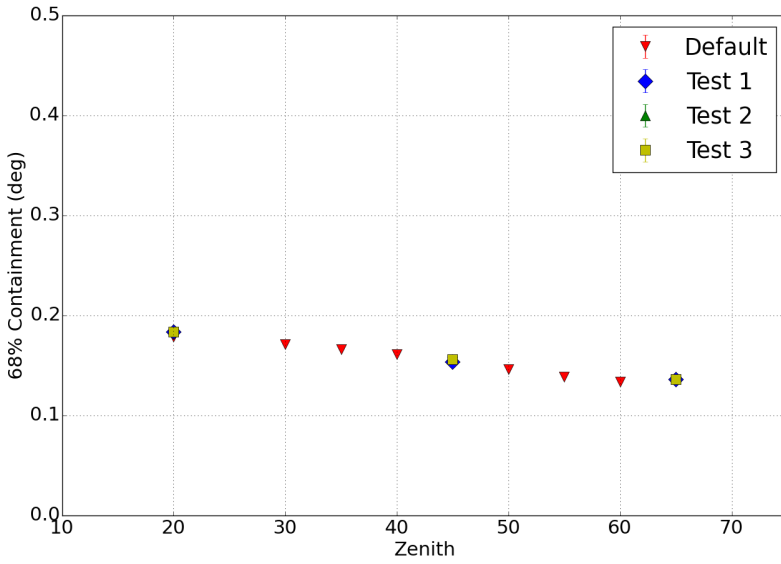
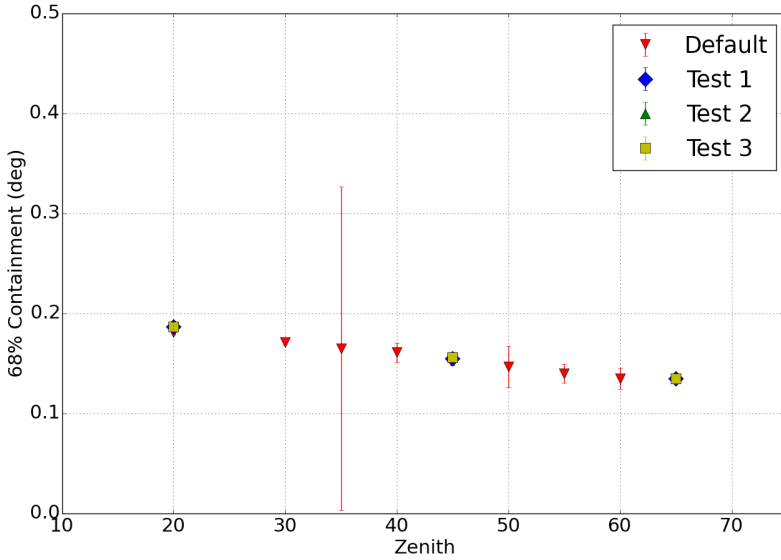


Figure 3.9: The functions used to assign relative weights to events as a function of angular distance from the camera center in the training samples in the new tables (Default, Test 1, Test 2 and Test 3) and those found in the scripts used to generate the older tables (Old Script 1, Old Script 2).

These tests reveal small changes in the R_{68} value despite large changes in the correction function (Fig. 3.10). This suggests that the *Disp* tables are not sensitive to changes in acceptance and therefore the different acceptance functions are unlikely to be the reason why the new *Disp* tables perform worse at smaller zenith angles.



(a) Numerically determined R_{68} .



(b) R_{68} as determined from a fit.

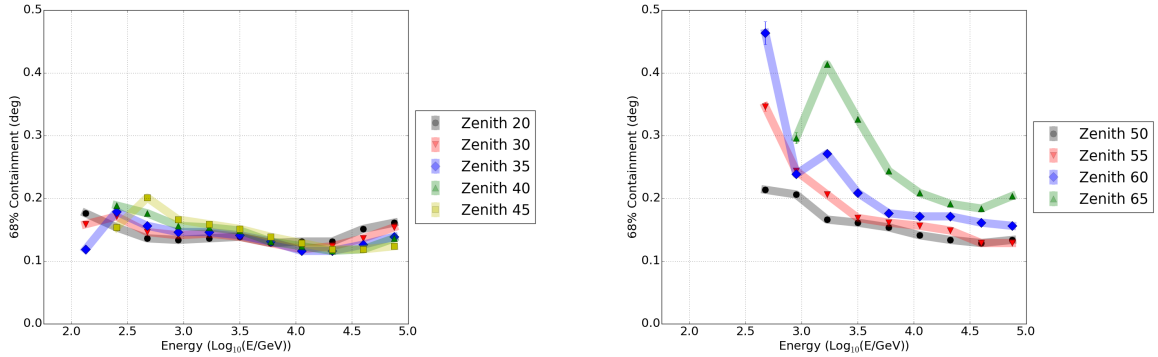
Figure 3.10: R_{68} for each acceptance correction function shown in Fig. 3.9 with the numerically determined R_{68} (top) and that found from the fit to two Gaussians (bottom). The changes in acceptance correction do not meaningfully change the R_{68} for the reconstruction. The large uncertainties in some of the fit values arise from the non-Gaussian shape of the overall distribution, and the long tails causing a poor fit to the superposition of two gaussians.

3.2.6 Energy Dependence

Another important dependence of the reconstruction resolution (and therefore the R_{68}) is that on energy. Higher energy photons are expected to comprise a larger fraction of LZA photons because lower energy showers suffer more absorption in the atmosphere.

Conversely, high energy photons make up a small fraction of SZA photons (and more generally, all cosmic photons) due to the $\sim E^{-2}$ shape of the spectrum. A better resolution at higher energy would also be expected to contribute to the improved resolution at LZA.

Due to the slicing in energy in addition to zenith and therefore smaller number statistics, this is expected to lead to relatively sparse data in each bin. For this reason, in this section we address only the R_{68} determined from the numerical integral, and not that from the fit.



(a) Energy Dependence of Method0 at small and (b) Energy Dependence of Method0 at large zenith angles.

Figure 3.11: Energy Dependence of Method0 with R_{68} for small zenith angles (left) and that for large zenith angles (right). Colored bands are intended to guide the eye and do not represent data points. The data bin at $\phi = 65$ and $\log_{10}(E/\text{GeV}) \sim 3.25$ appears to be consistently under-performing, this is an artifact from low statistics in this bin.

The Method0 energy dependence (Fig. 3.11) follows the same trend as in Fig. 2.2 – seeing the best resolution for all zenith angles in the 3-30TeV range as well as a low energy improvement likely driven by higher statistics. The energy dependence for the older *Disp*

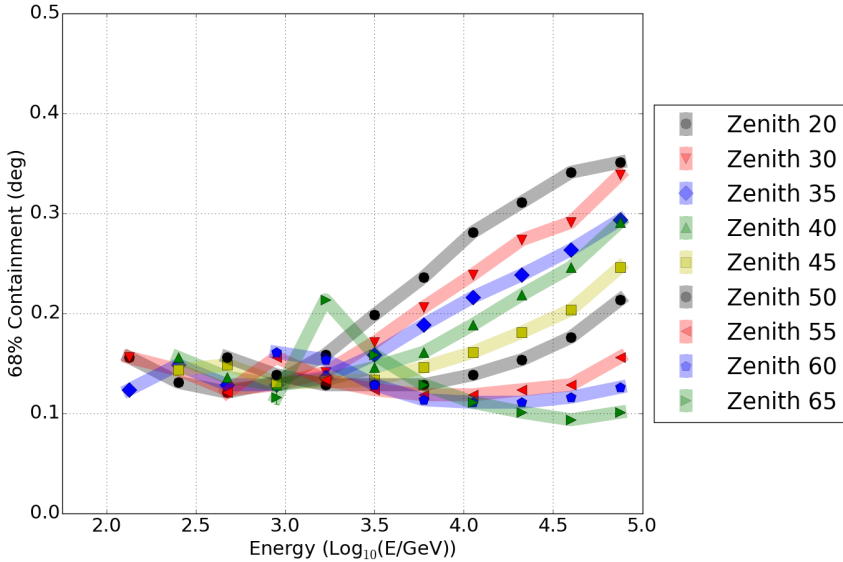


Figure 3.12: Energy Dependence of the old Method5t with the numerically determined R_{68} . Colored bands are intended to guide the eye and do not represent data points. The data bin at $\phi = 65$ and $\text{Log}_{10}(E/\text{GeV}) \sim 3.25$ appears to be consistently under-perform, this is an artifact from low statistics in this bin.

tables (Fig. 3.12) appears to have a minimum in R_{68} close to 1 TeV. These old *Disp* tables also see a degradation in resolution at the highest energies. The newer *Disp* tables (Fig. 3.13) on the other hand appear to do **better at higher energies for all zenith angles**. At energies above ~ 1 TeV and zenith angle greater than 30° , the R_{68} is at or better than 0.3° (see Fig. 3.14). Compared to the geometric method this provides major improvements in the LZA region (top rows of Fig. 3.15(a) and 3.16(a)) and compared to the older *Disp* tables, we see major improvements in the high energy-medium zenith regime (lower right corner of Fig. 3.15(b) and 3.16(b))

3.3 R_{68} for Observational Data and Known Objects

In order to test the validity of the results from the simulations, a known point-source with sufficient data collection at LZA and a hard spectrum (and therefore high statistics in the

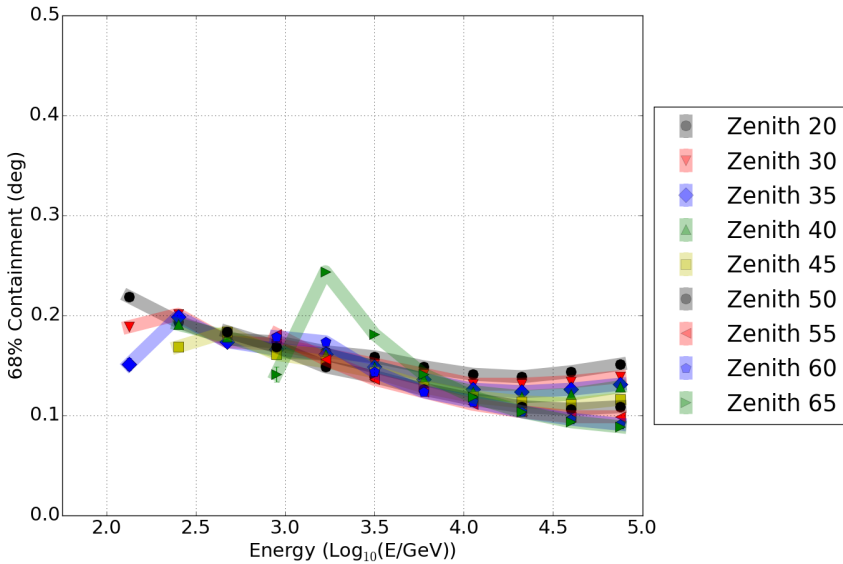


Figure 3.13: Energy Dependence of the new Method5t with the numerically determined R_{68} . Colored bands intended to guide the eye and do not represent data points. The data bin at $\phi = 65$ and $\text{Log}_{10}(E/\text{GeV}) \sim 3.25$ appears to be consistently under-perform, this is an artifact from low statistics in this bin.

TeV range) was needed. Since our initial test was performed on the Crab Nebula, the Crab was used to perform some validation tests. This was also useful since the Crab the known object with the longest total exposure time at LZA in VERITAS archival data and therefore was largest available dataset for performing these tests. Additionally, Mrk421 [25] was used as a known point source to test the power of discrimination between point and compact sources. Each of these objects and the corresponding analysis will be discussed in greater detail in the following sections.

3.3.1 Data Constraints and Li & Ma Significance

For the data analysis, unlike with the simulations, a “true” direction was not knowable. Instead, the true direction must be assumed to be that of the known object, and we must restrict our analysis to those showers determined to be from the source object, and where

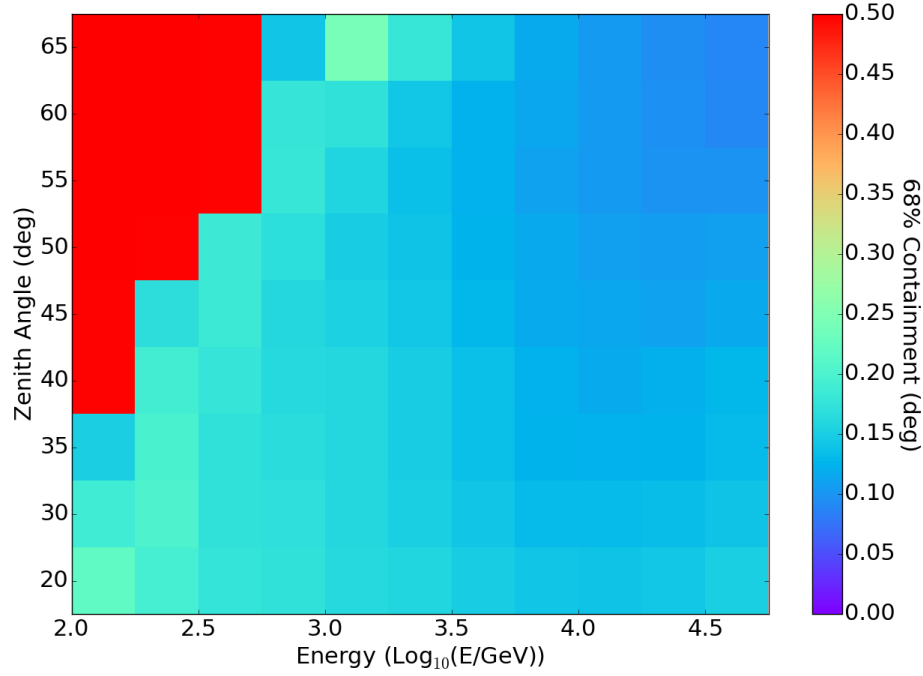


Figure 3.14: Energy and zenith dependence of the new Method5t, with colors denoting the R_{68} and red denoting $R_{68} \geq 0.50^\circ$. The upper-left corner shows regions of loss in resolution in the large-zenith low-energy region due to low statistics.

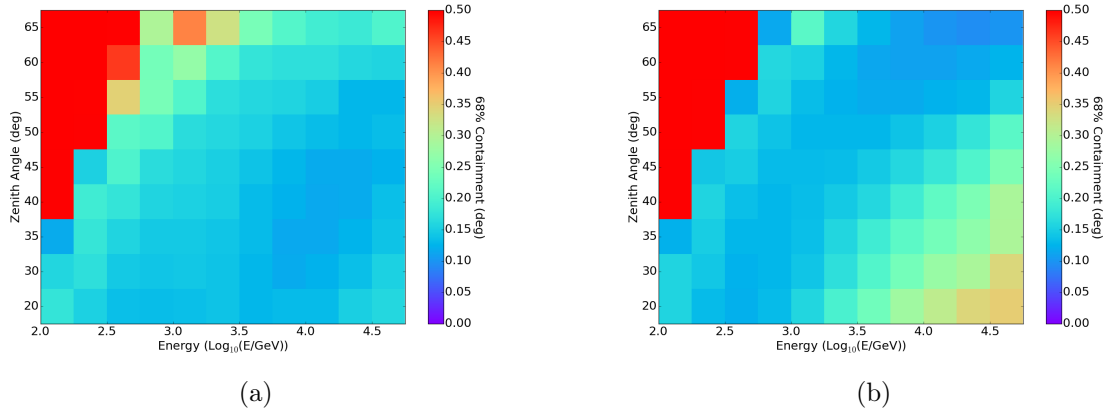


Figure 3.15: Energy and zenith dependence of the geometric reconstruction (left) and the old Method5t (right), with colors denoting the R_{68} and red denoting $R_{68} \geq 0.50^\circ$.

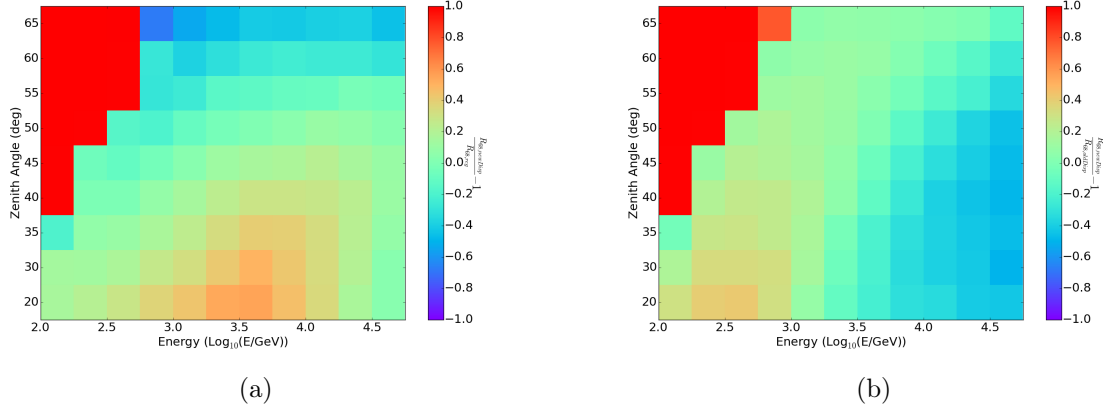


Figure 3.16: Performance of the new *Disp* method compared to Method0 (left) and the old *Disp* method (right), with purple at -1.0 denoting 100% improvement over the older method and bright red (in the upper left corners) at 1.0 denoting 100% worse performance in that bin or regions of insufficient statistics. The range of usefulness for Method5t (relative to Method0) now extends to $E \geq 1\text{TeV}$ and $\phi \gtrsim 55^\circ$ (upper-right corner).

the source object is in fact detected.

As a measure of detection, we use both the number of excess events – defined as the number of events determined to be from the source minus the number of events from the off-source regions scaled by the ratio of the exposures of the on and off-source regions. For a number of events from the source region N_{on} , a number of events from the off-source region N_{off} , and a ratio of exposure $\frac{A_{on}}{A_{off}} = \alpha$, the number of excess events is given by $N_{on} - \alpha N_{off}$. This corresponds to the number of events observed above the number expected given the background observation, and statements regarding the small- or large-number statistics refer to this number being small or large.

As a measure of the robustness of the R_{68} determined for the data, we also use the gamma-ray astronomy standard Li & Ma [26] significance, with a threshold significance of 3σ . A high significance measurement of the object in a given energy and zenith bin should provide a measure of R_{68} in that bin that is relatively stable against statistical fluctuations.

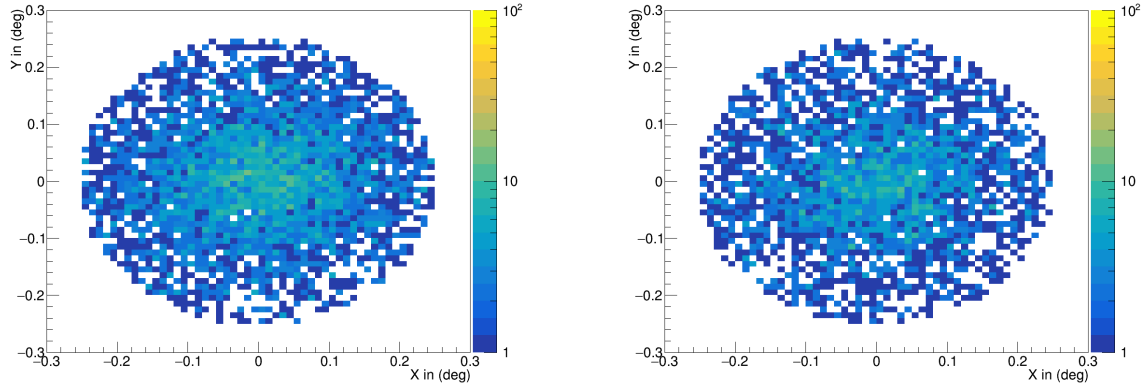
Lastly, as a measure of how the data analysis performs relative to expectations from

the simulation analysis we also use a direct bin-wise comparison of the resulting numerical R_{68} defined as $\xi = \frac{R_{68,\text{data}}}{R_{68,\text{sim}}} - 1$. This provides a numerical quantity that is expected to be zero and provides a simple percentage deviation from expectation. A ξ of 0.3 means the R_{68} from data in a given bin was 30% larger than that from simulations, with positive values signifying “under-performance” and negative values signifying “over-performance”.

3.3.2 R_{68} for the Crab Nebula

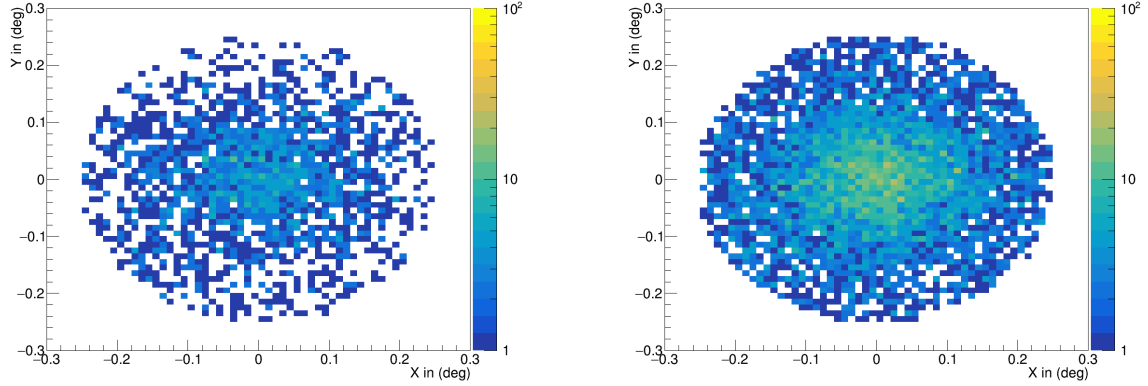
The Crab Nebula is measured to have a GeV-TeV extension of $\sim 0.03^\circ$ [27][28]. To observe this, a R_{68} of at least 0.03° is required which, based on the simulations, we do not achieve (see Fig. 3.13). This however provides another metric by which to quantify our resolution, as well as to measure possible future gains in resolution.

Fig. 3.17 shows skymaps for zenith cuts and energy cuts for the Crab data set with $\phi \geq 40^\circ$. This zenith cut was applied in order to only look at Crab data where it would be relevant to this analysis, since the Crab has several hundred hours of total data in the VERITAS archival dataset. This serves also to demonstrate the change between the dataset with $E \geq 1$ TeV and $\phi \geq 50$ and that with $E < 1$ TeV and $\phi < 50$ without the otherwise overwhelming effects of larger statistics in the low-energy small zenith angle region. With the colors providing a log-scale representation of the number of excess events at a given 2D deviation from the source location, we can see that Fig. 3.17(d) has more events closer to the center of the skymap than Fig. 3.17(a). It is however also clear that a more robust demonstration of this effect requires a higher significance dataset in the regions of interest.



(a) Crab skymap for $\phi < 50^\circ$ and $E < 1$ TeV.

(b) Crab skymap for $\phi \geq 50^\circ$ and $E < 1$ TeV.



(c) Crab skymap for $\phi < 50^\circ$ and $E \geq 1$ TeV.

(d) Crab skymap for $\phi \geq 50^\circ$ and $E \geq 1$ TeV.

Figure 3.17: Reconstruction of the Crab direction using Method5t and with data runs such that the mean zenith angle was $\phi \geq 40^\circ$, with the colors providing a log-scale representation of the number of excess events at a given 2D deviation from the source location. We can see that (d) has more events closer to the center of the skymap than (a), and while a similar effect may be visible in (b) and (c), those effects are washed out by small statistics and low significance.

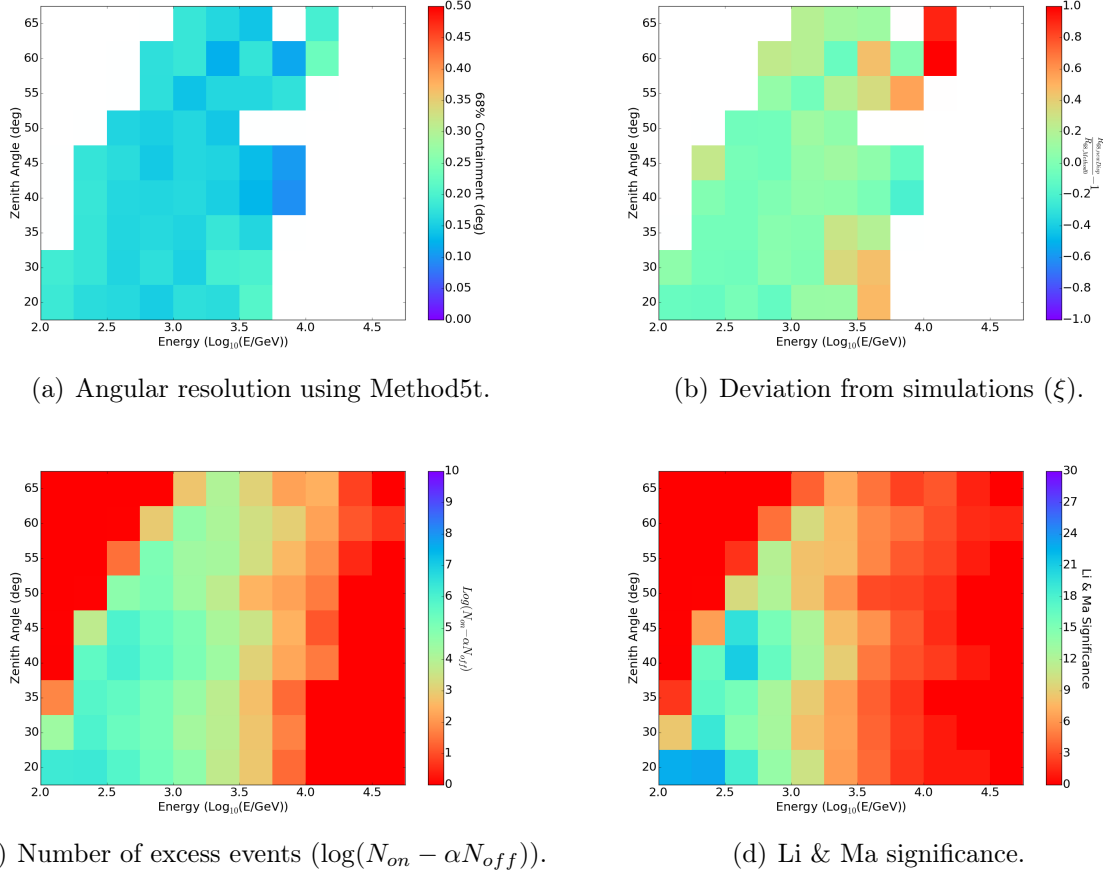


Figure 3.18: Reconstruction of the direction of the Crab Nebula horizon-to-horizon runs using the new *Disp* tables. In the top two plots, white denotes regions of significance $< 3\sigma$. Relative to Fig. 3.3, this provides better resolution at the highest zenith angles, and is able to reconstruct higher-energy events in the $45 - 55^\circ$ region.

Relative to Fig. 3.3, this provides better resolution at the highest zenith angles and is able to reconstruct higher-energy events in the $45 - 55^\circ$ region. This provides a proof-of-principle that the *Disp* method is an improvement on the standard method at the highest energies and at large zenith angles. In the region $\phi \geq 50$ and $E \geq 1$ TeV the Crab nebula has a R_{68} of $\sim 0.15^\circ$.

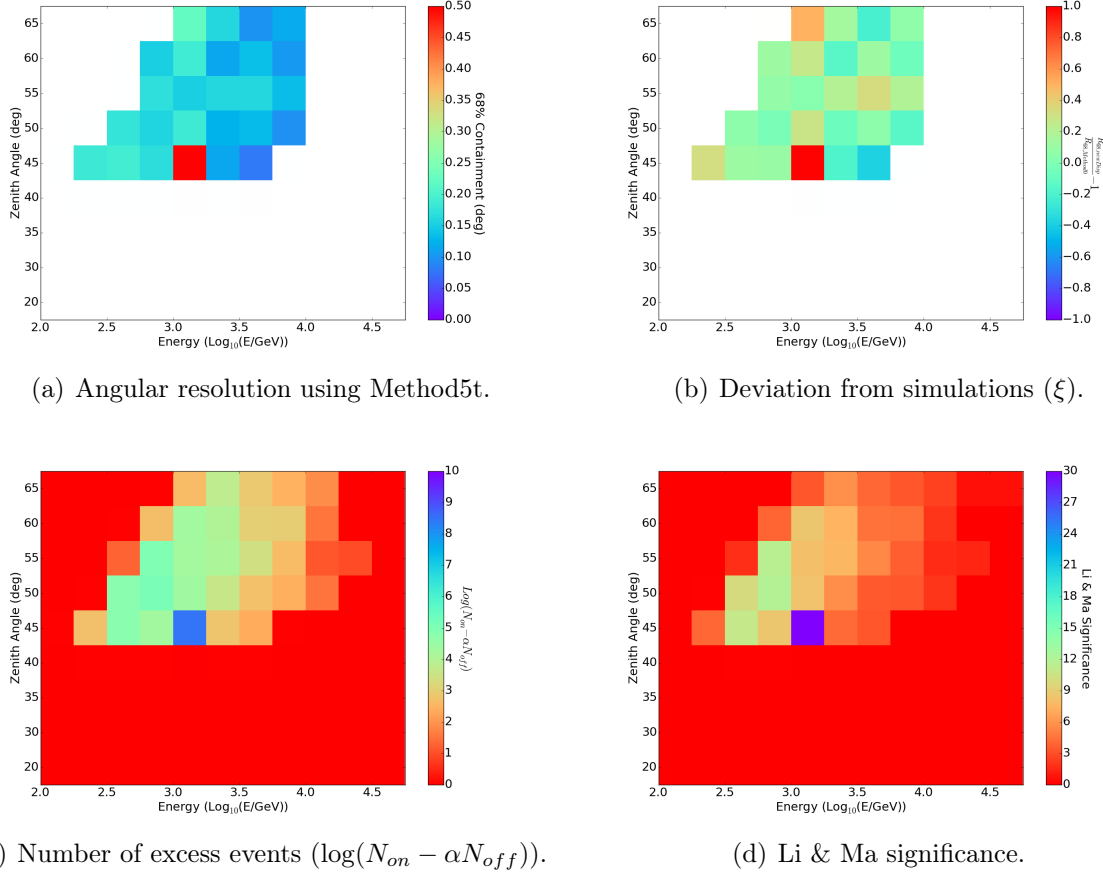


Figure 3.19: Reconstruction of the direction of the Crab Nebula LZA runs using the new *Disp* tables. In the top two plots, white denotes regions of significance $< 3\sigma$.

The numbers for the Crab Nebula in Fig. 3.18 suggest that we can not yet detect the extension of the Crab, which is consistent with the simulation analysis. Also expected from the simulation results, the R_{68} decreases with increasing energy. In the regime of interest, ($E > 1$ TeV and $\phi \gtrsim 50^\circ$), the data reconstruction under-performs relative to simulations with $\xi \sim 0.3$, and the dependence of the R_{68} (see Fig. 3.19(a)) on zenith angle is smaller than expected. This is perhaps due to lower statistics in the region (see Fig. 3.19(c)), since for most of our parameter space, $|\xi| \leq 0.15$ (Fig. 3.19(b)).

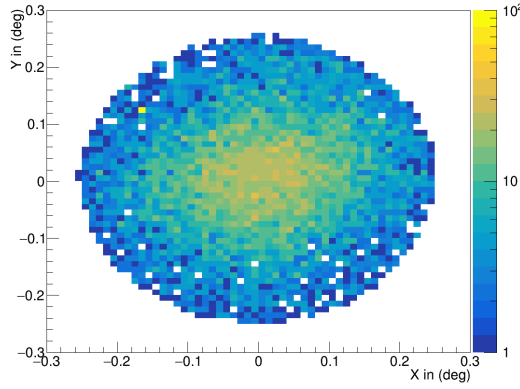
3.3.3 R_{68} for Mrk421

Mrk421 is an extra-galactic source ($z = 0.031$) with a hard spectrum (spectral index $\Gamma = 2.2$ [29]), but less than 5 hours of observation in the zenith range of interest ($\phi > 45^\circ$). Even with a short total duration of observation, because Mrk421 is a high-flux object [30], it is still observable at high significance. In the region $\phi \geq 50$ and $E \geq 1$ TeV Mrk 421 has a R_{68} of $\sim 0.11^\circ$.

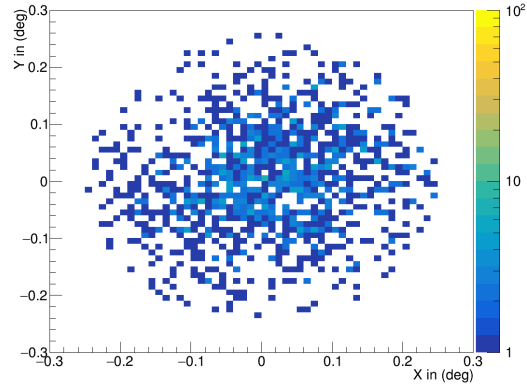
Fig. 3.20 shows skymaps for zenith cuts and energy cuts for the Mrk421 data set with $\phi \geq 15^\circ$. This zenith cut was not as tight as that used for the Crab data because the Mrk421 data was used to validate the simulation results across a larger range of zenith angles. This plot is meant to demonstrate the change in R_{68} between the dataset with $E \geq 1$ TeV and $\phi \geq 50$ and that with $E < 1$ TeV and $\phi < 50$, but the low significance in the high-zenith and high-energy regions means that statements about trends in R_{68} are not very robust.

With the colors providing a log-scale representation of the number of photons at a given 2D deviation from the source location, we can see that Fig. 3.20(c) has more events closer to the center of the skymap than Fig. 3.20(a) and a similar trend is visible between Fig. 3.20(b) and Fig. 3.20(d). It is however also clear that a more robust demonstration of this effect requires a higher significance dataset in the regions of interest.

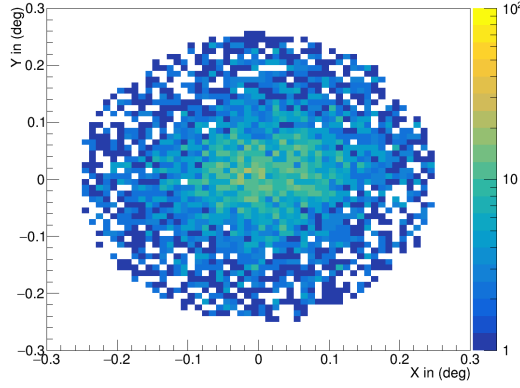
The result of this analysis was that the smallest values of R_{68} for Mrk421 ($\sim 0.09^\circ$, Fig. 3.21(a)) are found in a region of parameter space where the Li & Ma significance is small (Fig. 3.21(d)) and more generally that the high values of ξ are found where Li & Ma significance is low, suggesting that a more robust analysis would require more statistics. Consequently this point-source analysis does not definitively validate the results from the simulations but it does demonstrate the simulation result that the point-source reconstruction in the regime of interest is $< 0.2^\circ$ (Fig. 3.21(a)).



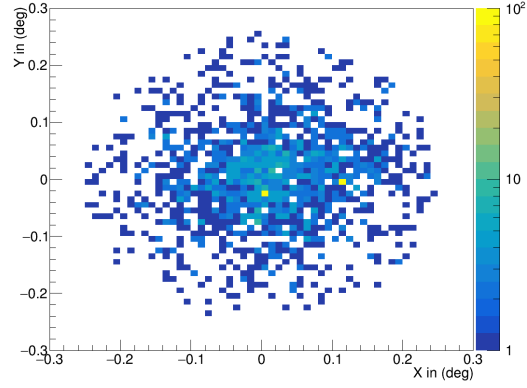
(a) Crab skymap for $\phi < 50^\circ$ and $E < 1$ TeV.



(b) Crab skymap for $\phi > 50^\circ$ and $E < 1$ TeV.



(c) Crab skymap for $\phi < 50^\circ$ and $E > 1$ TeV.



(d) Crab skymap for $\phi > 50^\circ$ and $E > 1$ TeV.

Figure 3.20: Reconstruction of the Mrk421 direction using Method5t, with color denoting number of excess events in log scale. There is a visible increase in number of events in the center of the skymap relative to the edges with an increase in energy (from (a) to (c) and (b) to (d)), but any conclusive statement regarding this trend requires better statistics.

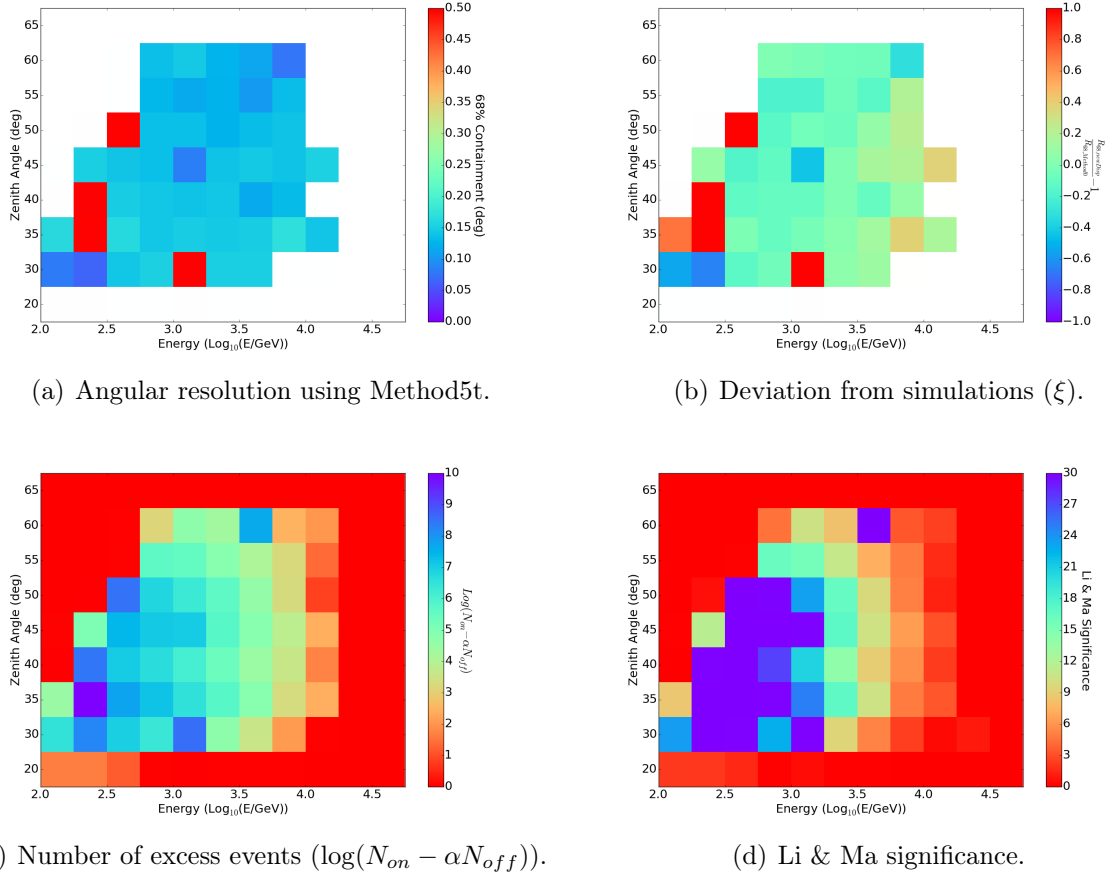


Figure 3.21: Reconstruction of the direction of Mrk421 using the new *Disp* tables. In the top two plots, white denotes regions of significance $< 3\sigma$.

Chapter 4

Conclusions

4.1 Summary

The purpose of this work was to study and refine the *Disp* method, as well as to study the explicit and implicit dependencies of the reconstruction using this method. This revealed that:

- The *Disp* method is significantly better than the standard method of reconstruction at $\phi \gtrsim 45^\circ$.
- The angular 68% containment for the new *Disp* tables is at the level of 0.3° or better for energies above 1 TeV and zenith angles greater than 30° , and at the level of 0.15° for energies above ~ 3 TeV and zenith angles greater than 40° . At the largest zenith angles ($> 55^\circ$), this constitutes **improvements of 30-50%** in angular resolution (see Fig. 3.16).
- The angular 68% containment is independent of noise level in the training and testing sample.

- The angular 68% containment is independent of the camera acceptance correction (for offset from the center of the camera face) used in the training.
- The angular 68% containment is strongly dependent on energy with the expected trend - improving with both energy and zenith angle up to constraints placed by low statistics.
- While the new *Disp* tables appear to perform worse than the older Disp tables in the small and medium zenith angle ranges (as measured by the 68% containment), **the improvements in the LZA ranges are significant**. The performance in the small-medium zenith angle range is not a major concern since the standard method performs as well or better in these energy ranges and requires fewer resources.
- The results obtained from an analysis of known objects are largely within 15% of those expected from the simulations. The angular reconstruction resolution determined from the Monte Carlo simulations, when tested using known source objects (Crab, Mrk 421), shows that (for $\phi \geq 50$ and $E \geq 1$ TeV) Mrk 421 has a 68% containment of $\sim 0.11^\circ$ and that (for $\phi \geq 50$ and $E \geq 1$ TeV) the Crab has a 68% containment of 0.15° .

4.2 Future Work

The data reconstruction deviates from the simulation reconstruction significantly, based on the currently available observed dataset. Part of this may be a question of small number statistics, and this could be probed by using small-number sub-samples of the simulation data-set and looking at the ξ for the data. Alternatively, there may be a systematic energy-related mis-characterization of photons as “on-source” in the data leading to a bias towards the tails. Other explanations could be in the deviation from Gaussianity in the simulations themselves, which themselves merit a closer look.

Bibliography

- [1] L. A. et. al. Antonelli. The Next Generation of Cherenkov Telescopes. A White Paper for the Italian National Institute for Astrophysics (INAF). *arXiv e-prints*, page arXiv:0906.4114, Jun 2009.
- [2] T. C. et. al. Weekes. Observation of TeV gamma rays from the Crab nebula using the atmospheric Cerenkov imaging technique. *The Astrophysical Journal*, 342:379–395, jul 1989.
- [3] CTA collaboration. C.T.A. website.
<https://www.cta-observatory.org/science/gamma-rays-cosmic-sources/>.
- [4] Nahee Park. Status of ground based gamma-ray observations. *PoS*, ICRC2017:1116, 2018.
- [5] Giuseppe Di Sciascio. Ground-based Gamma-Ray Astronomy: an Introduction. *J. Phys. Conf. Ser.*, 1263(1):012003, 2019.
- [6] MAGIC collaboration. MAGIC website. <https://magic.mpp.mpg.de/>.
- [7] HESS collaboration. H.E.S.S. website.
<https://www.mpi-hd.mpg.de/hfm/HESS/pages/home/som/2005/10/>.
- [8] VERITAS collaboration. VERITAS website. <https://veritas.sao.arizona.edu/>.

- [9] VERITAS collaboration. VERITAS website, specifications page.
[https://veritas.sao.arizona.edu/about-veritas-mainmenu-81/
 veritas-specifications-mainmenu-111](https://veritas.sao.arizona.edu/about-veritas-mainmenu-81/veritas-specifications-mainmenu-111).
- [10] T. C. Weekes et al. VERITAS: Very energetic radiation imaging telescope array system. *AIP Conf. Proc.*, 515(1):515, 2000. [5,173(2000)].
- [11] S. Mollerach and E. Roulet. Progress in high-energy cosmic ray physics. *Progress in Particle and Nuclear Physics*, 98:85–118, Jan 2018.
- [12] Cherenkova, Elena P. The discovery of the Cherenkov radiation. *Nucl. Instrum. Meth.*, A595:8–11, 2008.
- [13] I. M. Frank and I. E. Tamm. Coherent visible radiation of fast electrons passing through matter. *Compt. Rend. Acad. Sci. URSS*, 14(3):109–114, 1937. [Usp. Fiz. Nauk93,no.2,388(1967)].
- [14] LA et. al. Antonelli. The Next Generation of Cherenkov Telescopes. A White Paper for the Italian National Institute for Astrophysics (INAF). *arXiv preprint arXiv:0906.4114*, 2009.
- [15] J. M. Davies and E. S. Cotton. Design of the quartermaster solar furnace. *Solar Energy*, 1:16–22, April 1957.
- [16] Dave B. Kieda. The Gamma Ray Detection sensitivity of the upgraded VERITAS Observatory. In *Proceedings, 33rd International Cosmic Ray Conference (ICRC2013): Rio de Janeiro, Brazil, July 2-9, 2013*, page 0700, 2013.
- [17] A. M. Hillas. Cerenkov light images of EAS produced by primary gamma. *International Cosmic Ray Conference*, 3, August 1985.
- [18] W. Hofmann. Data analysis techniques for stereo IACT systems. *AIP Conf. Proc.*, 515(1):318–322, 2000.

- [19] D. Heck. Extensive air shower simulations with CORSIKA and the influence of highenergy hadronic interaction models. In *From e^+e^- to Heavy Ion Collisions: Proceedings of the 30th International Symposium on Multiparticle Dynamics (ISMD 2000), Tihany, Hungary, October 9-15, 2000*, pages 252–259, 2000.
- [20] Stephane Vincent. A Monte Carlo template-based analysis for very high definition imaging atmospheric Cherenkov telescopes as applied to the VERITAS telescope array. *PoS*, ICRC2015:844, 2016.
- [21] Mathieu de Naurois and Loïc Rolland. A high performance likelihood reconstruction of γ -rays for imaging atmospheric Cherenkov telescopes. *Astroparticle Physics*, 32:231–252, Dec 2009.
- [22] Cogan, P. VEGAS, the VERITAS Gamma-ray Analysis Suite. 3:1385, 2007.
- [23] Gernot Maier and Jamie Holder. Eventdisplay: An Analysis and Reconstruction Package for Ground-based Gamma-ray Astronomy. *PoS*, ICRC2017:747, 2018. [35,747(2017)].
- [24] CERN collaboration. CERN ROOT website. <https://root.cern.ch/>.
- [25] M. et. al. Punch. Detection of TeV photons from the active galaxy Markarian 421. *Nature*, 358(6386):477–478, Aug 1992.
- [26] T.-P. Li and Y.-Q. Ma. Analysis methods for results in gamma-ray astronomy. *The Astrophysical Journal*, 272:317–324, Sep 1983.
- [27] M. Ackermann et al. The Search for Spatial Extension in High-latitude Sources Detected by the *Fermi* Large Area Telescope. *Astrophys. J. Suppl.*, 237(2):32, 2018.
- [28] M. Holler, D. Berge, J. Hahn, D. Khangulyan, R. D. Parsons, and H. E. S. S. Collaboration. Advanced search for the extension of unresolved TeV sources with H.E.S.S. *International Cosmic Ray Conference*, 35:676, January 2017.

- [29] J. et. al. Albert. Observations of Markarian 421 with the MAGIC Telescope. *The Astrophysical Journal*, 663:125–138, July 2007.
- [30] M. L. et. al. Ahnen. Long-term multi-wavelength variability and correlation study of Markarian 421 from 2007 to 2009. *Astronomy and Astrophysics*, 593:A91, September 2016.